MAMKO: MAMBA-BASED KOOPMAN OPERATOR FOR MODELING AND PREDICTIVE CONTROL

Zhaoyang Li[1], **Minghao Han**[2], **Xunyuan Yin**[1,2,*]
1 School of Chemistry, Chemical Engineering and Biotechnology, Nanyang Technological University
2 Nanyang Environment and Water Research Institute, Nanyang Technological University
LIZH0082@e.ntu.edu.sg; minghao.han@ntu.edu.sg; xunyuan.yin@ntu.edu.sg

ABSTRACT

The Koopman theory, which enables the transformation of nonlinear systems into linear representations, is a powerful and efficient tool to model and control nonlinear systems. However, the ability of the Koopman operator to model complex systems, particularly time-varying systems, is limited by the fixed linear state-space representation. To address the limitation, the large language model, Mamba, is considered a promising strategy for enhancing modeling capabilities while preserving the linear state-space structure. In this paper, we propose a new framework, the Mamba-based Koopman operator (MamKO), which provides enhanced model prediction capability and adaptability, as compared to Koopman models with constant Koopman operators. Inspired by the Mamba structure, MamKO generates Koopman operators from online data; this enables the model to effectively capture the dynamic behaviors of the nonlinear system over time. A model predictive control system is then developed based on the proposed MamKO model. The modeling and control performance of the proposed method is evaluated through experiments on benchmark time-invariant and time-varying systems. The experimental results demonstrate the superiority of the proposed approach. Additionally, we perform ablation experiments to test the effectiveness of individual components of MamKO. This approach unlocks new possibilities for integrating large language models with control frameworks, and it achieves a good balance between advanced modeling capabilities and real-time control implementation efficiency.

1 INTRODUCTION

Deep learning methods have made promising achievements in modeling large and complex systems with collected datasets (Wang et al., 2024). The time-series prediction tasks can be well achieved with existing learning technologies and applied to various fields, including weather forecasting (Verma et al., 2024) and traffic prediction (Li et al., 2023). These data-driven methods, especially for deep learning methods, have proven to be highly capable of modeling dynamic systems and provide strong support for advanced control applications.

The Koopman operator theory (Koopman, 1931) has emerged as a promising data-driven method in recent years. The Koopman operator can represent the dynamics of nonlinear systems by linear state-space model (SSM) (Kalman, 1960) by lifting the states from the original space to a higher-dimensional space through a series of observable functions. Based on the theory, extended dynamic mode decomposition (EDMD) (Williams et al., 2015) with manually selected observable functions is proposed. With the advent of deep learning, neural networks (NNs) have been employed to serve as the observable functions in the Koopman operator framework. Advanced deep learning methods, such as autoencoders (Takeishi et al., 2017), probabilistic NNs (Han et al., 2021), and graph NNs (Li et al., 2020), have been integrated with the Koopman operator to enhance the prediction accuracy of the model. The linear controller based on the Koopman model, including linear quadratic regulator (Han et al., 2023), can be efficiently designed from the concise linear model. Although the Koopman model mentioned above shows relatively accurate prediction results, due to the parameter capacity

*Corresponding author: Xunyuan Yin.

of the Koopman framework, challenges still exist in modeling real-world systems, especially for time-varying systems.

Large language models (LLMs) (Zhao et al., 2023) are deep learning models that leverage a large-scale number of parameters to comprehend and generate human language. The internal architecture of the model enables it to link and reason through contextual information. The most typical structure inside the large language model is Transformer (Wolf et al., 2020). Although the nonlinear function and attention mechanism (Vaswani et al., 2017) primarily improve the approximation capacity, the intricate structures pose challenges for model-based controller design. The Mamba structure (Gu & Dao, 2023) based on SSM is developed for LLMs. Within the structure of Mamba, the similar linear SSM from Koopman operator theory is interpreted as a particular form that integrates features from both recurrent neural networks (RNNs) and convolutional neural networks (CNNs) (Dao & Gu, 2024). Selection mechanisms from Mamba are implemented to improve the modeling ability of linear SSM by generating matrix sequences, which can also be a potential solution for improving the capacity of the Koopman model.

In this work, we propose a Mamba-based Koopman operator (MamKO) by integrating the matrices generation network from Mamba (Gu & Dao, 2023) with the original Koopman model to enhance the modeling accuracy. The structure can generate the Koopman operators according to the historical data and construct the SSM accordingly. Using the linear SSM, the MPC problem is formulated as a convex optimization problem. The proposed methods are then evaluated against existing representative approaches across various settings. The results demonstrate the superiority of the proposed framework in both modeling and control performance compared to state-of-the-art methods. The contributions of this work are summarized as follows:

- We propose a novel Mamba-based Koopman operator (MamKO) modeling method, which leverages matrices generated from the Mamba structure to model complex nonlinear systems.
- We further enhance the matrix generation structure of Mamba to accommodate unstable and time-varying systems.
- We develop an MPC scheme based on the MamKO model to achieve computationally efficient optimal control of nonlinear systems.
- Experiments are conducted on benchmark time-invariant and time-varying systems to illustrate the efficacy and superiority of the proposed framework.

2 Related works

Koopman Operators Koopman operator theory (Koopman, 1931) has been regarded as a powerful tool for dynamic system analysis (Brunton et al., 2022). In (Schulze et al., 2022), the scope of Koopman operator theory is extended from autonomous systems to controlled systems, enabling the design of corresponding controllers. Methods with manually selected observable functions show promising results in both modeling and control (Zhang et al., 2023). However, the time consumption to find appropriate observable functions is a significant drawback of this approach. An alternative method using NNs to automatically construct the observable functions can bypass this problem. This kind of Koopman model has been effectively applied in areas such as fluid physics (Morton et al., 2018), robotics (Shi & Meng, 2022), chemical engineering (Han et al., 2024a), and vehicle systems (Chen & Lv, 2024), where the neural network-based model serves as a powerful predictor.

Although the Koopman model has received much attention and is well-studied both in the field of modeling and control, challenges still exist when facing complex systems, especially for time-varying systems. (Zhang et al., 2019) has developed an online dynamic mode decomposition strategy for time-varying systems with slowly changing parameters. With the online collected data, (Hao et al., 2022) designs an adjusting algorithm to tune the parameters in the observable functions. Integrating with the Fourier filter to disentangle and exploit time-invariant and time-varying dynamics, the Koopman operators are updated in (Liu et al., 2023) to accommodate the time-varying dynamics. While these methods have shown promising results, the optimization process within the online updating framework can be time-consuming and may lead to infeasible solutions. In contrast, our approach directly generates the Koopman operators from historical data, enabling real-time production of the time-varying SSM.

Mamba Structure Previous works on Mamba are based on the research of state-space model (Gu et al., 2020; 2022b) for continuous data processing and applied to the field of audio and vision (Goel et al., 2022; Nguyen et al., 2022). The structured state-space sequence models (S4) (Gu et al., 2022a) are expanded to selective state-space models (S6) in (Gu & Dao, 2023) by adding the selection mechanism. The mechanism inside the Mamba structure transfers the time-invariant model to the time-varying model by generating the matrices of SSMs using the input data, which can facilitate the modeling of time-varying tasks. The modeling ability has largely increased with this mechanism, and a corresponding hardware-aware algorithm has been proposed to boost computational efficiency further. The Mamba structure has been applied in the fields including language processing (Lieber et al., 2024), image segmentation (Zhu et al., 2024; Ruan & Xiang, 2024), video processing (Li et al., 2024). Notably, while the Mamba structure is based on a linear SSM, it is not directly suitable for controller design due to nonlinear functions within the selection mechanism. Modifications have been introduced to adapt the system to fit within the control framework.

Model-based Learning Control With the development of data-driven methods, the modeling accuracy has increased, facilitating the application of model-based learning control methods. In the field of model-based reinforcement learning, multiple algorithms have been proposed to train the control strategy inside the established model (Ha & Schmidhuber, 2018; Hafner et al., 2019; 2020; 2023). From the perspective of MPC, the computational burden for optimization problems is an important issue for model-based learning control. Some machine learning methods are preferred for lightweight use. Stochastic MPC based on Gaussian regression are discussed in (Hewing et al., 2019; 2020). Gaussian regression is applied to learn unknown disturbances inside the systems, which improves the robustness of the controller. From the collected input-output trajectories, a linear model can be constructed in the form of the Hankel matrix and helps to generate optimal control output (Berberich et al., 2020). Neural network-based models have also been integrated into the MPC framework (Chen et al., 2019; Nubert et al., 2020). However, the computational burden becomes a significant concern as the modeling accuracy improves from the intricate structures. In this work, we incorporate the Mamba structure and Koopman operator theory to balance modeling performance with control efficiency.

3 MODELING

In this section, the basic concepts of the Koopman operator will first be introduced. Then, the derivation of the Mamba-based Koopman operator (MamKO) is presented.

3.1 THE KOOPMAN OPERATOR

In typical Koopman-based approaches, a general time-invariant controlled nonlinear system is considered presented as:

$$x_{k+1} = f(x_k, u_k) \tag{1}$$

where $x_k \in \mathcal{X} \subset \mathbb{R}^n$ is the state vector at time instant k; $u_k \in \mathcal{U} \subset \mathbb{R}^m$ denotes the input vector of the system at time instant k; f is a nonlinear function describing the dynamic behavior of the nonlinear system. The Koopman theory proposed in Koopman (1931) shows that there exists an infinite-dimensional Koopman operator $\mathcal{K} : \mathcal{H} \to \mathcal{H}$ acting on the observable functions such that the dynamics of the nonlinear process in (1) can be linearly represented, which can be formulated as:

$$\mathcal{K}\psi(x_k, u_k) = \psi \circ f(x_k, u_k) = \psi(x_{k+1}) \tag{2}$$

where ψ denotes the observable functions and $\circ$ represents function composition. From an application point of view, it is favorable to approximate Koopman operators on a finite-dimensional function space $\overline{\mathcal{H}} \subset \mathcal{H}$. Considering the Koopman operator design in (Korda & Mezić, 2018), the system in (1) modeled by Koopman operator can be formulated as:

$$\begin{aligned} z_{k+1} &= Az_k + Bu_k \\ \hat{x}_k &= Cz_k \end{aligned} \tag{3}$$

where $z_k = \psi(x_k)$ denotes the shifted state vector in $\overline{\mathcal{H}}$ via the observable function $\psi : \mathbb{R}^n \to \mathbb{R}^N$. The corresponding finite-dimensional Koopman operator is split into $A \in \mathbb{R}^{N\times N}$ and $B \in \mathbb{R}^{N\times m}$. The details for learning the Koopman operator are included in Appendix A.

3.2 MAMBA-BASED KOOPMAN OPERATOR

For real-world applications, the formulation in (1) could fail in modeling systems where the future states are not only dependent on the current state and inputs but also on time. The parameters or structures of the systems can change over time. A more general form considering the influence of time can be formulated as:

$$x_{k+1} = f(x_k, u_k, k), \tag{4}$$

At a given time instant k, the time-varying nonlinear system in (4) can be regarded as a time-invariant system in (1). Thus, the dynamics at each time instant can be represented by the Koopman model in (3), which implies that a distinct set of matrices $\{A, B, C\}$ can capture the dynamics at a specific time instant. However, as time proceeds, the matrices $\{A, B, C\}$ for the previous instant will not be sufficient for describing the dynamics at the current instant. An effective approach to model this time-varying system involves identifying a set of matrices A_k, B_k, C_k for each time instant k, which adapts to the changing dynamics. The corresponding linear time-varying SSM can capture the dynamics of the system for each time instant, which can be formulated as:

$$\begin{aligned} z_{k+1} &= A_k z_k + B_k u_k \\ \hat{x}_k &= C_k z_k \end{aligned} \tag{5}$$

where $z_k = \psi(x_k)$ represents the shifted state vector. Some parameters from observable function ψ_k and Koopman operators A_k, B_k, and C_k should be updated online to accommodate time-varying systems. Some research has been dedicated to updating parameters in ψ_k, A_k, B_k, and C_k using online-collected datasets. In (Hao et al., 2022; Chen et al., 2024; Zhang et al., 2019), the Koopman operators or observable functions are optimized online to approximate the dynamics reflected in the newly collected data. Although these methods can provide good performance, solving the corresponding online optimization problems can be time-consuming and even infeasible. Instead, in our approach, we resort to the Mamba structure, which contains a generative framework for matrices, to enable timely real-time updates of the Koopman matrices.

Mamba Structure Mamba (Gu & Dao, 2023), a large language model based on the state-space model, provides a promising frame for modeling time-varying systems. Compared with the S4 framework (Gu et al., 2022a) for time-invariant systems, the selection mechanism is included to generate matrices from the input sequence, which formulated the time-varying SSM.

Inspired by the SSM model from the Mamba framework, we aim to develop a generative approach to compute the time-varying Koopman operators over the prediction horizon. However, directly applying the Mamba framework for the modeling and predictive control task is impractical. When considering the system in (5), the Mamba framework only focuses on the inputs u in the form of the word sequence, while states in the LLMs do not have exact meaning. However, for a controlled system in (4), the states and inputs with physical meaning should all be considered. Meanwhile, in (5), as B_k is generated from the input sequence containing u_k, the bilinear term $B_k u_k$ can lead to a non-convex optimization problem for in the control part. As a substitute, we generate the matrices from the historical data. The differences between the proposed framework and the Mamba framework are discussed in Appendix B.

Matrices Generation Inspired by the Mamba framework, we utilize discretization to generate matrices efficiently. Given the matrices A, B in the continuous system and the sampling period T, the discrete matrices $\bar{A}$, $\bar{B}$ can be calculated by the zero-order hold (ZOH) as:

$$\begin{aligned} \bar{A} &= e^{AT} \\ \bar{B} &= \int_0^T e^{At} \mathrm{d}t \cdot B \end{aligned} \tag{6}$$

The matrix A is set as a diagonal matrix, facilitating the discretization process. In the Mamba framework, the diagonal elements of A are constrained to be negative through a negative exponential function to promote the stability of the SSM. However, not all real-world systems are inherently stable, such as the oscillator system (Elowitz & Leibler, 2000). This constraint can significantly compromise modeling accuracy. In our work, we address this problem by substituting the negative exponential function with a negative continuously differentiable exponential linear unit (CELU) (Barron, 2017). The formulation of CELU can be presented as:

$$CELU(x) = \max(0, x) + \min(0, \alpha(e^{(\frac{x}{\alpha})} - 1)) \tag{7}$$

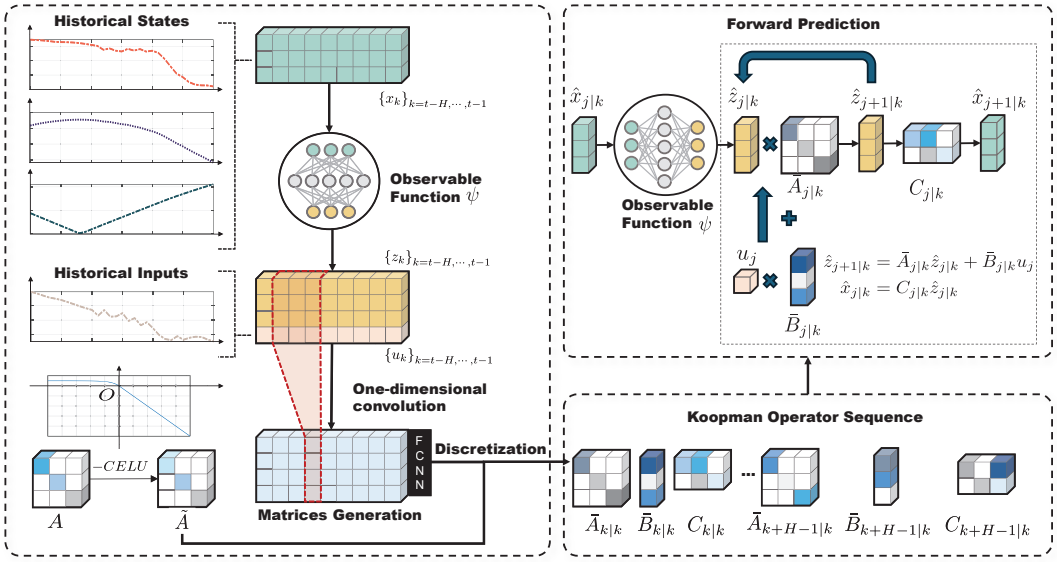

Figure 1: Structure of the MamKO. With the matrices generation network and the observable function, the linear time-varying SSM can be established. By transforming the initial state to the shifted state through the observable function ψ, the linear time-varying SSM can produce a sequence of the future states.

where $\alpha = 1$ in this paper. The CELU is continuously differentiable, which can lead to smooth gradient updates. As CELU can generate negative output, the negative CELU allows for the existence of positive eigenvalues, thereby facilitating the representation of unstable systems. The new diagonal matrix activated by CELU is denoted as $\tilde{A}$, with the eigenvalues limited in the range of $[-\infty, 1]$.

At time instant k, the historical state sequence $x_{k-H:k-1}$ from the past H steps is shifted to space $\overline{\mathcal{H}}$ through the observable function ψ, obtaining the shifted state sequence $z_{k-H:k-1}$. The combination of shifted state sequence and historical input sequence forms the historical data sequence $\left[z_{k-H:k-1}^{\mathrm{T}}, u_{k-H:k-1}^{\mathrm{T}}\right]^{\mathrm{T}}$. One-dimensional convolution is implemented in the historical data sequence to extract the temporal information inside. The extracted feature c_i can be calculated by:

$$c_i = w\left[z_{i:i+h-1}^{\mathrm{T}}, u_{i:i+h-1}^{\mathrm{T}}\right]^{\mathrm{T}} + b, i = k-H, \ldots, k-h \tag{8}$$

where w and b are the weight and bias parameters in the convolution network, and h is the kernel size. The matrix sequences $B_{k:k+H-1}$ and $C_{k:k+H-1}$ and the sampling periods sequence $T_{k:k+H-1}$ are encoded from the extracted features using fully connected NNs (FCNNs). Discretizing $\tilde{A}$, $B_{k:k+H-1}$ using sampling periods sequence $T_{k:k+H-1}$ by (6), the obtained matrix sequences $\bar{A}_{k:k+H-1}$, $\bar{B}_{k:k+H-1}$ and $C_{k:k+H-1}$ are applied to the Koopman framework to accomplish multi-step-ahead prediction tasks via the model in (5) recursively. The structure of the proposed MamKO is presented in Figure 1.

Optimization Procedure The observable function that projects the state vector to finite-dimensional function space is denoted as $\psi(\cdot|\theta_\psi)$ with trainable parameters θ_ψ. The matrices generation networks can be denoted as $\phi(\cdot|\theta_\phi)$ with trainable parameters θ_ϕ. The networks take the data sequence $\left[z_{k-H:k-1}^{\mathrm{T}}, u_{k-H:k-1}^{\mathrm{T}}\right]^{\mathrm{T}}$ and trainable matrix A as input, and produce matrix sequence $\bar{A}_{k:k+H-1|k}$, $\bar{B}_{k:k+H-1|k}$ and $C_{k:k+H-1|k}$. To effectively train the matrix A, parameters θ_ψ and θ_ϕ, the optimization problem for multi-step-ahead prediction tasks should be designed. Given the dataset

$\{x_j, u_j\}_{j=k-H,\cdots,k+H}$, the optimization can be formulated as follows:

$$\min_{A,\theta_\psi,\theta_\phi} \frac{1}{H}\sum_{j=k+1}^{k+H} \|\hat{x}_{j|k} - x_j\|_2^2 \tag{9a}$$

$$\text{s.t. } \hat{z}_{j+1|k} = \bar{A}_{j|k}\hat{z}_{j|k} + \bar{B}_{j|k}u_j \tag{9b}$$

$$\hat{z}_{k|k} = \psi(x_k|\theta_\psi) \tag{9c}$$

$$\hat{x}_{j|k} = C_{j|k}\hat{z}_{j|k} \tag{9d}$$

$$\tilde{A} = -CELU(A) \tag{9e}$$

$$z_j = \psi(x_j|\theta_\psi), j = k-H, \cdots, k-1 \tag{9f}$$

$$\bar{A}_{k:k+H-1|k}, \bar{B}_{k:k+H-1|k}, C_{k:k+H-1|k} = \phi(\tilde{A}, z_{k-H:k-1}, u_{k-H:k-1}|\theta_\phi) \tag{9g}$$

where $\hat{z}_{j|k}$ represents the predicted shifted state vector for time instant j at time instant k; $\hat{x}_{j|k}$ represents the state vector for time instant j predicted at time instant k; H represents the length of the model's prediction horizon. $\bar{A}_{k:k+H-1|k}$, $\bar{B}_{k:k+H-1|k}$ and $C_{k:k+H-1|k}$ are the generated matrix sequences from the historical data sequence. To minimize the prediction loss in (9a), all parameters are updated with gradient descent using ADAM (Kingma, 2014).

4 CONTROL

In this section, for the time-varying system in (4), we propose a model predictive control framework that is inspired by Korda & Mezić (2018) based on the MamKO model.

At each time instant k, the matrix sequences $\bar{A}_{k:k+H-1|k}$, $\bar{B}_{k:k+H-1|k}$ and $C_{k:k+H-1|k}$ for prediction are generated previously with the historical data. With the matrix sequence, the optimization problem for MPC is formulated as follows:

$$\min_{u^*_{k|k},\ldots,u^*_{k+H-1|k}} \sum_{j=k+1}^{k+H-1} \left(\|C_{j|k}\hat{z}_{j|k} - x_s\|_Q^2 + \|u_{j|k} - u_{j-1|k}\|_R^2\right) + \|C_{k+H|k}\hat{z}_{k+H|k} - x_s\|_P^2 \tag{10a}$$

$$\text{s.t.} \quad z_{j+1|k} = \bar{A}_{j|k}\hat{z}_{j|k} + \bar{B}_{j|k}u_{j|k} \tag{10b}$$

$$\hat{z}_{k|k} = \psi(x_k) \tag{10c}$$

$$C\hat{z}_{j|k} \in \mathcal{X} \tag{10d}$$

$$u_{j|k} \in \mathcal{U}, j = k+1, \ldots, k+H-1 \tag{10e}$$

where $u^*_{k|k}, \ldots, u^*_{k+N-1|k}$ denotes the trajectory of optimal control signals determined given the current time instant k; $\|\cdot\|_Q^2$ denotes a vector's squared weighted Euclidean norm, which is computed by $\|x\|_Q^2 = x^TQx$; Q, R and P are positive-definite weighting matrices; $\|C_{j|k}\hat{z}_{j|k} - x_s\|_Q^2$ and $\|C_{k+H|k}\hat{z}_{k+H|k} - x_s\|_P^2$ are used to reduce tracking errors; $\|u_{j|k} - u_{j-1|k}\|_R^2$ is set to improve the smoothness of the control inputs; (10b) serves as the model constraint; (10c) provides the initial condition in the shifted state-space; (10d) and (10e) are state and input constraints, respectively. At time instant $k \geq 0$, the optimal control input trajectory is calculated and the first element of the trajectory, $u^*_{k|k}$ is applied to the nonlinear process in (4) as the control input for the current time instant. The convex optimization problems derived from linear SSMs can be efficiently solved.

5 EXPERIMENTS

In this section, we will evaluate the performance of the MamKO model in terms of modeling and control. Specifically, we evaluate the following aspects: (a) **Convergence** of the proposed training algorithm on different systems with random parameter initialization. (b) **Model accuracy** of the MamKO compared to other methods in time-invariant and time-varying systems. (c) **Control performance** of the MPC based on the MamKO compared to other methods in time-invariant and time-varying systems.

Five benchmark systems are included to evaluate the modeling and control performance of the MamKO. The CartPole balancing system is included as a benchmark system for the controller design task, which has been widely used in deep reinforcement learning (DRL) research (Lillicrap, 2015; Haarnoja et al., 2018). Correspondingly, a time-varying CartPole balancing system described in (Hao et al., 2022) is considered to test the performance of MamKO on the time-varying system. Moreover, we apply the MamKO to the biological gene regulatory networks (GRN) (Elowitz & Leibler, 2000). The complex nonlinear systems in the chemical engineering field are also considered. The reactor-separator chemical process (Yin & Liu, 2019) comprising two continuous stirred tank reactors and a flash tank separator is chosen as a benchmark chemical process, denoted as the reactor-separator chemical process (RSCP) system. We also simulate the reactor-separator process with time-varying parameters (Nikravesh et al., 2000), denoted as the time-varying RSCP system.

For the modeling performance evaluation, we compare the proposed method with two competitive baseline methods. **(1)** The Deep Koopman Operator (DKO) (Lusch et al., 2018; Han et al., 2020) is a Koopman method that employs deep NNs in constructing the observable functions. Different from the generative Koopman operators from MamKO, the Koopman operators in the DKO are invariant. **(2)** The Multilayer Perceptrons (MLP) (Chua et al., 2018), based on multilayer fully connected NNs, is implemented as a baseline for modeling the systems.

For the control performance evaluation, we compare the MamKO-based MPC with three state-of-the-art baseline methods: **(1)** The DKO-based MPC (Lusch et al., 2018; Han et al., 2020); **(2)** MLP-based MPC, which utilizes the NNs as predictive models and solves a nonlinear optimization with the help of Casadi (Andersson et al., 2019) and Interior Point Optimizer, pronounced eye-pea-Opt (IPOPT) (Wächter & Biegler, 2006); **(3)** Soft actor-critic (SAC) (Haarnoja et al., 2018), which is a state-of-the-art model-free reinforcement learning algorithm. Despite the higher sample complexity of model-free methods compared to model-based ones, SAC often achieves superior control performance. SAC updates the controller to minimize cumulative stage costs, thereby implicitly optimizing for a stabilizing controller.

For each environment, trajectories of state and action samples are gathered, generating a training set of $36,000$ samples, a validation set of $4,000$ samples, and a test set of $4,000$ samples. Specifically, actions are uniformly sampled from the action space for each time instant for the CartPole system, the time-varying CartPole system, and the GRN system. For the RSCP and time-varying RSCP systems, actions are determined using a step function with added random noise. Details of the experimental setup are provided in Appendix C. The methods are trained to predict state sequences over a 30-step horizon. Hyperparameters for each method are listed in Appendix D. For the SAC control task, each environment undergoes training with 1000k steps of state-action-reward pairs.

5.1 Modeling evaluation

The losses for the modeling task are calculated by the average prediction error of each step on the test set. For each system, we run ten model training trials with different datasets and randomly initialized parameters to test the convergence of the algorithms. The results for each system are presented in Figure 2 (a-e). In comparison to DKO, MamKO demonstrates superior modeling accuracy across all environments. Especially for the two time-varying systems, the MamKO outperforms the other two methods. Notably, with the nonlinear structures from the NNs, the MLP has fewer prediction errors in GRN and RSCP. Nonetheless, the inherent nonlinearities of the MLP model may complicate optimization tasks, leading to reduced computational efficiency and suboptimal behavior. The experiments in the next section will show the possible limitations of MLP in controller design.

Performance on the rapidly changing dynamics For the time-varying CartPole system in (Hao et al., 2022), a time-varying coefficient of the friction of the cart is added to the system in the form of sine waves. Based on the example, we compare the modeling performance of the three methods with different frequencies of the sine waves. The time-varying Cartpole system described before has the angular frequency of 1 rad/s. Two time-varying Cartpole systems with the angular frequencies of 0.1 rad/s and 10 rad/s are added. The results are shown in Figure 2 (f), illustrating that as the angular frequency of the time-varying parameters increases, the advantages of using MamKO become more pronounced. The generative matrices provide a more accurate representation of the system with rapidly changing parameters, as different matrices approximate the dynamics of systems at each time instant.

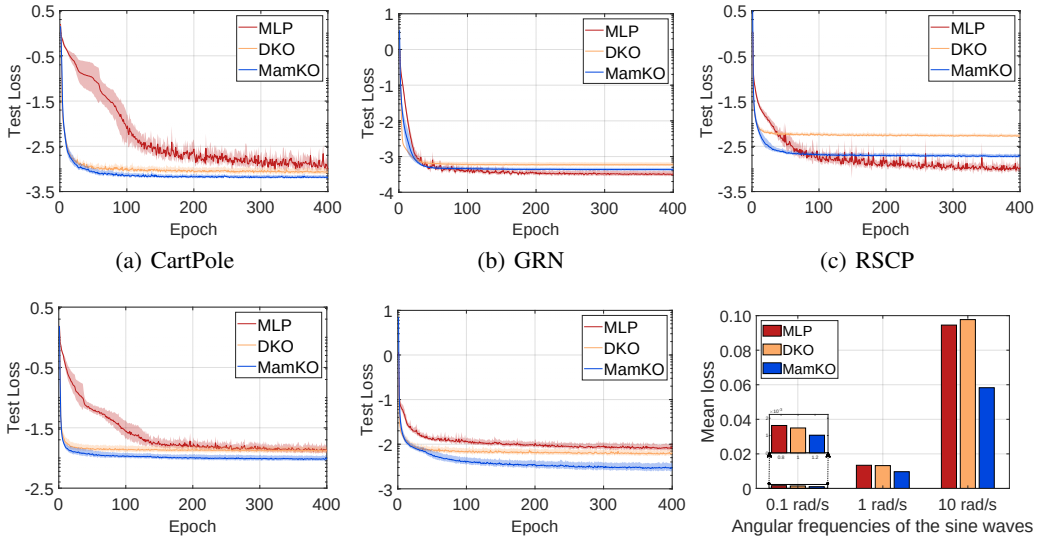

(a) CartPole (b) GRN (c) RSCP

(d) Time-varying CartPole (e) Time-varying RSCP (f) Time-varying CartPole with different parameters

Figure 2: Average prediction error on the test set (a-e) and average prediction error for the time-varying CartPole with different coefficients (f). In (a-e), the Y-axis indicates the average mean-squared prediction error in log space for the 30-step-ahead prediction task, and the X-axis indicates the training epochs. The shaded area represents the confidence interval (0.5 times the standard deviation)
across ten training trials. In (f), the Y-axis indicates the average loss after training for 400 epochs.

5.2 CONTROL EVALUATION

The control performance of the four methods is evaluated and compared in the five systems. The time-varying CartPole with the angular frequency of 10 rad/s is included to evaluate the control performance for the system with rapidly changing dynamics. The control task for each environment is set-point tracking, and the details can be found in Appendix C. The weighting parameters Q, R, and P for the MPCs are carefully adjusted to reach the best performance of each baseline method. The prediction horizon is set as 30 for all MPCs.

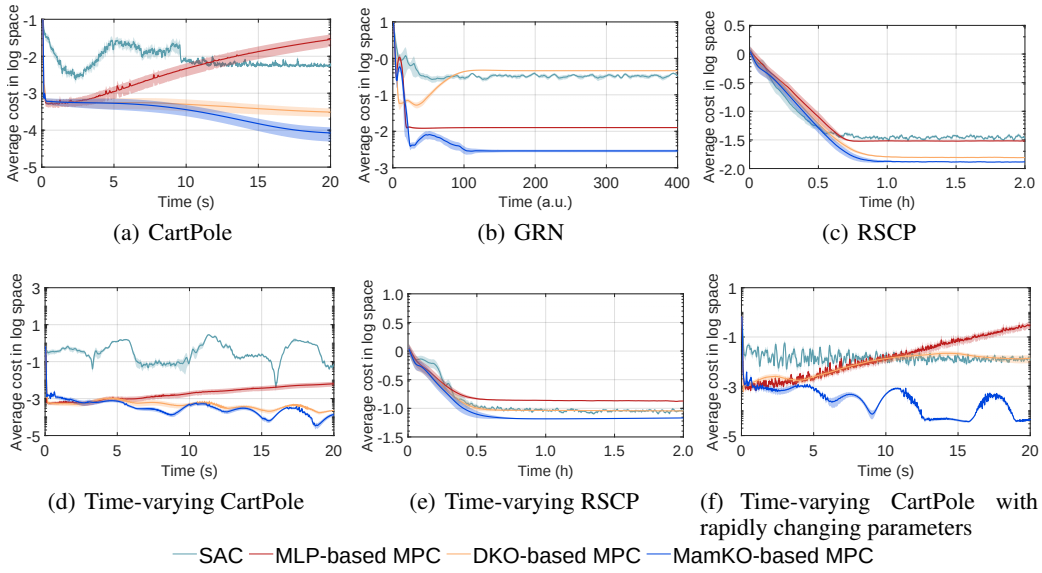

(a) CartPole (b) GRN (c) RSCP

(d) Time-varying CartPole (e) Time-varying RSCP (f) Time-varying CartPole with rapidly changing parameters

Figure 3: Average cost based on track error. The Y-axis indicates the average cost in log space for ten experiments with random initial states. The shaded area represents the confidence interval (0.3 times the standard deviation) over the ten experiments.

The cost trajectories are shown in Figure 3. The state trajectories can be found in Appendix F. As shown in Figure 3, the MamKO-based MPC achieves the best control performance for all five systems. In comparison with DKO-based MPC, the MamKO-based MPC reduces the cost of the five systems by 5.05%, 3.70%, 92.10%, 6.56%, 14.19%, 84.74%, respectively. A significant improvement is observed in the time-varying CartPole with rapidly changing parameters. Although MLP achieves better modeling performance on GRN and RSCP systems, the corresponding control performance is not as good as its modeling performance, which can be attributed to suboptimal solutions from the non-convex optimization problems. Compared with the SAC, the two Koopman model-based MPCs can all achieve a relatively stable control performance for the time-varying system. Although it can be hard to construct a time-varying model, the Koopman operator in DKO can construct an average Koopman operator that accommodates various time-varying parameters in the systems, which can provide relatively good results.

5.3 Evaluation on the activation function

As we simplify A as a diagonal matrix, the eigenvalues of the matrix become the trainable parameters directly. Compared to the Mamba framework, which sets the eigenvalues to be negative, we replace the original negative exponential function with the negative CELU function. In this section, we will compare the modeling performance of MamKO using the negative exponential function, the negative CELU function, and no activation function on the CartPole system, the GRN system, and the RSCP system. As observed in Figure 4, the MamKO with CELU function has the best modeling performance.

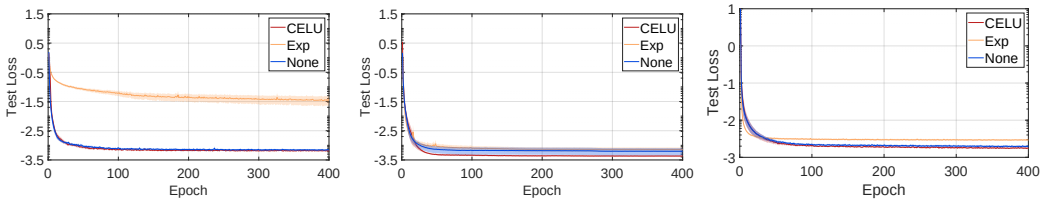

(a) CartPole (b) GRN (c) RSCP

Figure 4: Evaluation on the activation function for the eigenvalues. For the CartPole system, the MamKO with the negative CELU function performs slightly better than the one without the activation function and largely better than the one with the negative exponential function. For the GRN and RSCP systems, the MamKO with the negative CELU has the smallest mean loss and lowest variance. Compared with the MamKO with no activation function, the improvement of the MamKO with the negative CELU is not significant. However, the initiation of A of the MamKO with no activation function should be carefully adjusted since no constraint is added to the eigenvalues. Otherwise, too large eigenvalues may result in unstable gradient descent.

5.4 Ablation on the discretization

We also evaluate the impact of discretization on modeling performance. The benefit of generating the sequence of the Koopman operator through the method in (6) is demonstrated in this subsection. We compare the performance of this modeling approach with another method that applies the same discretization technique to matrix B as to matrix A, which is $\bar{B} = e^{BT}$. The pipeline is named as $Multiplication$. The modeling results for each environment are presented in Table 1. From Table 1, we can find that with the discretization on the matrices following (6), the modeling accuracy can be significantly improved, which validates the effect of the discretization.

Table 1: Results of the ablation on the discretization.

Method	**CartPole**	**GRN**	**RSCP**	**Time-varying CartPole**	**Time-varying RSCP**
Discretization	6.50×10^{-4}	1.91×10^{-3}	2.92×10^{-3}	4.31×10^{-4}	9.67×10^{-3}
Multiplication	8.30×10^{-4}	3.52×10^{-3}	7.60×10^{-3}	9.11×10^{-4}	1.19×10^{-2}

5.5 EVALUATION ON THE COMPUTATION TIME

In this subsection, we evaluate the computation time of the control methods on different benchmark systems. The online control implementation of the control methods is conducted on a computer equipped with an Intel Core i9-13900K CPU and 128 GB DDR4 RAM. The computation times of the MamKO-based MPC and baselines during control on the benchmark systems are presented in Table 2. Compared with the MLP-based MPC, the MamKO-based MPC reduces the computation time by 98.38%, 83.39%, 99.21%, 90.34%, 99.17% for the five benchmark systems, respectively. To further demonstrate the computational efficiency of the proposed method, the sampling periods of the systems are presented in Table 3. A comparison of the sampling periods and computation times demonstrates that the proposed MamKO-based MPC method can reliably ensure online implementation for each of the considered systems. The efficient online implementation of the proposed method stems from the use of a linear state-space model within the proposed framework, which facilitates the formulation of an optimal control problem that requires solving convex optimization despite the nonlinearity in the dynamics of the considered systems.

Table 2: Results of the computational time of each method in the benchmark systems.

Method	CartPole	GRN	RSCP	Time-varying CartPole	Time-varying RSCP
MLP-based MPC	7.43×10^{-1} s	1.09×10^{-1} s	3.31 s	1.74×10^{-1} s	3.45 s
DKO-based MPC	7.35×10^{-3} s	1.41×10^{-2} s	1.06×10^{-2} s	7.63×10^{-3} s	1.28×10^{-2} s
MamKO-based MPC	1.02×10^{-2} s	1.81×10^{-2} s	2.62×10^{-2} s	1.68×10^{-2} s	2.95×10^{-2} s
SAC	2.67×10^{-4} s	3.23×10^{-4} s	3.41×10^{-4} s	2.68×10^{-4} s	3.32×10^{-4} s

Table 3: Sampling periods of the benchmark systems.

Method	CartPole	GRN	RSCP	Time-varying CartPole	Time-varying RSCP
Sampling period	0.02 s	1 s	18 s	0.02 s	18 s

The results also indicate that the extended computation time required by the MLP-based MPC, which is due to the need to solve nonlinear optimization problems, poses challenges for its online implementation. This limitation is particularly critical for systems with fast dynamics and short sampling periods, and for larger-scale systems with numerous control inputs and state variables to optimize.

6 CONCLUDING REMARKS

In this paper, a new modeling and control framework called Mamba-based Koopman Operator (MamKO) was proposed by seamlessly integrating the Koopman operator with the large language model Mamba. The matrices generation network from Mamba was adapted to construct the linear time-varying state-space model based on the Koopman modeling concept. The MamKO model can effectively predict the future states of nonlinear systems with time-varying parameters. A model predictive controller was formulated based on the established MamKO model. Both time-invariant and time-varying benchmark systems were leveraged to evaluate the modeling and control performance of the proposed method. The experiments demonstrated the superior performance of the MamKO model in both modeling and control tasks. Future work will focus on applying the MamKO model to large-scale systems to further evaluate its modeling capabilities.

Future research directions include the formal analysis of the convergence and stability of the proposed MamKO-based control approach and the utilization of the MamKO-based modeling framework for energy optimization of energy-intensive industrial systems, for example, through integrating the proposed modeling framework with Koopman-based economic model predictive control (Han et al., 2024b). We also plan to investigate the application of the MamKO-based control methods to industrial systems of larger scales and more complex dynamics for efficient and robust system operations.

ACKNOWLEDGMENTS

This research is supported by the National Research Foundation, Singapore, and PUB, Singapore's National Water Agency under its RIE2025 Urban Solutions and Sustainability (USS) (Water) Centre of Excellence (CoE) Programme, awarded to Nanyang Environment & Water Research Institute (NEWRI), Nanyang Technological University, Singapore (NTU). This research is also supported by Ministry of Education, Singapore, under its Academic Research Fund Tier 1 (RS15/21 & RG63/22). Any opinions, findings and conclusions or recommendations expressed in this material are those of the author(s) and do not reflect the views of the National Research Foundation, Singapore, and PUB, Singapore's National Water Agency.

REFERENCES

Jens Alex, Lorenzo Benedetti, JB Copp, KV Gernaey, Ulf Jeppsson, Ingmar Nopens, MN Pons, Leiv Rieger, Christian Rosen, JP Steyer, et al. Benchmark simulation model no. 1 (BSM1). *Report by the IWA Taskgroup on benchmarking of control strategies for WWTPs*, 1, 2008.

Joel A. E. Andersson, Joris Gillis, Greg Horn, James B. Rawlings, and Moritz Diehl. CasADi – A software framework for nonlinear optimization and optimal control. *Mathematical Programming Computation*, 11(1):1–36, 2019.

Jonathan T Barron. Continuously differentiable exponential linear units. *arXiv preprint arXiv:1704.07483*, 2017.

Julian Berberich, Johannes Köhler, Matthias A Müller, and Frank Allgöwer. Data-driven model predictive control with stability and robustness guarantees. *IEEE Transactions on Automatic Control*, 66(4):1702–1717, 2020.

Greg Brockman, Vicki Cheung, Ludwig Pettersson, Jonas Schneider, John Schulman, Jie Tang, and Wojciech Zaremba. OpenAI Gym. *arXiv preprint arXiv:1606.01540*, 2016.

Steven L Brunton, Marko Budišić, Eurika Kaiser, and J Nathan Kutz. Modern Koopman theory for dynamical systems. *SIAM Review*, 64(2):229–340, 2022.

Hao Chen and Chen Lv. Incorporating ESO into deep Koopman operator modeling for control of autonomous vehicles. *IEEE Transactions on Control Systems Technology*, 32(5):1854–1864, 2024.

Tianze Chen, Yongqiang Huang, and Yu Sun. Accurate pouring using model predictive control enabled by recurrent neural network. In *IEEE/RSJ International Conference on Intelligent Robots and Systems*, pp. 7688–7694. IEEE, 2019.

Zhong Chen, Xiaofang Chen, Jinping Liu, Lihui Cen, and Weihua Gui. Learning model predictive control of nonlinear systems with time-varying parameters using Koopman operator. *Applied Mathematics and Computation*, 470:128577, 2024.

Kurtland Chua, Roberto Calandra, Rowan McAllister, and Sergey Levine. Deep reinforcement learning in a handful of trials using probabilistic dynamics models. In *Advances in Neural Information Processing Systems*, volume 31, 2018.

Tri Dao and Albert Gu. Transformers are SSMs: Generalized models and efficient algorithms through structured state space duality. *arXiv preprint arXiv:2405.21060*, 2024.

Michael B Elowitz and Stanislas Leibler. A synthetic oscillatory network of transcriptional regulators. *Nature*, 403(6767):335–338, 2000.

Karan Goel, Albert Gu, Chris Donahue, and Christopher Re. It's Raw! Audio generation with state-space models. In *International Conference on Machine Learning*, volume 162, pp. 7616–7633. PMLR, 2022.

Albert Gu and Tri Dao. Mamba: Linear-time sequence modeling with selective state spaces. *arXiv preprint arXiv:2312.00752*, 2023.

Albert Gu, Tri Dao, Stefano Ermon, Atri Rudra, and Christopher Ré. Hippo: Recurrent memory with optimal polynomial projections. In *Advances in Neural Information Processing Systems*, volume 33, pp. 1474–1487, 2020.

Albert Gu, Karan Goel, and Christopher Ré. Efficiently modeling long sequences with structured state spaces. In *International Conference on Learning Representations*, 2022a.

Albert Gu, Isys Johnson, Aman Timalsina, Atri Rudra, and Christopher Ré. How to train your HiPPO: State space models with generalized orthogonal basis projections. *arXiv preprint arXiv:2206.12037*, 2022b.

David Ha and Jürgen Schmidhuber. World models. *arXiv preprint arXiv:1803.10122*, 2018.

Tuomas Haarnoja, Aurick Zhou, Pieter Abbeel, and Sergey Levine. Soft actor-critic: Off-policy maximum entropy deep reinforcement learning with a stochastic actor. In *International Conference on Machine Learning*, pp. 1861–1870. PMLR, 2018.

Danijar Hafner, Timothy Lillicrap, Jimmy Ba, and Mohammad Norouzi. Dream to control: Learning behaviors by latent imagination. *arXiv preprint arXiv:1912.01603*, 2019.

Danijar Hafner, Timothy Lillicrap, Mohammad Norouzi, and Jimmy Ba. Mastering atari with discrete world models. *arXiv preprint arXiv:2010.02193*, 2020.

Danijar Hafner, Jurgis Pasukonis, Jimmy Ba, and Timothy Lillicrap. Mastering diverse domains through world models. *arXiv preprint arXiv:2301.04104*, 2023.

Minghao Han, Jacob Euler-Rolle, and Robert K Katzschmann. Desko: Stability-assured robust control with a deep stochastic Koopman operator. In *International Conference on Learning Representations*, 2021.

Minghao Han, Kiwan Wong, Jacob Euler-Rolle, Lixian Zhang, and Robert K. Katzschmann. Robust learning-based control for uncertain nonlinear systems with validation on a soft robot. *IEEE Transactions on Neural Networks and Learning Systems*, pp. 1–15, 2023.

Minghao Han, Zhaojian Li, Xiang Yin, and Xunyuan Yin. Robust learning and control of time-delay nonlinear systems with deep recurrent Koopman operators. *IEEE Transactions on Industrial Informatics*, 20(3):4675–4684, 2024a.

Minghao Han, Jingshi Yao, Adrian Wing-Keung Law, and Xunyuan Yin. Efficient economic model predictive control of water treatment process with learning-based Koopman operator. *Control Engineering Practice*, 149:105975, 2024b.

Yiqiang Han, Wenjian Hao, and Umesh Vaidya. Deep learning of Koopman representation for control. In *IEEE Conference on Decision and Control*, pp. 1890–1895. IEEE, 2020.

Wenjian Hao, Bowen Huang, Wei Pan, Di Wu, and Shaoshuai Mou. Deep Koopman learning of nonlinear time-varying systems. *arXiv e-prints*, pp. arXiv–2210, 2022.

Lukas Hewing, Juraj Kabzan, and Melanie N Zeilinger. Cautious model predictive control using Gaussian process regression. *IEEE Transactions on Control Systems Technology*, 28(6):2736–2743, 2019.

Lukas Hewing, Kim P Wabersich, Marcel Menner, and Melanie N Zeilinger. Learning-based model predictive control: Toward safe learning in control. *Annual Review of Control, Robotics, and Autonomous Systems*, 3(1):269–296, 2020.

Rudolph Emil Kalman. A new approach to linear filtering and prediction problems. 1960.

Diederik P Kingma. Adam: A method for stochastic optimization. *arXiv preprint arXiv:1412.6980*, 2014.

Bernard O Koopman. Hamiltonian systems and transformation in Hilbert space. *Proceedings of the National Academy of Sciences*, 17(5):315–318, 1931.

Milan Korda and Igor Mezić. Linear predictors for nonlinear dynamical systems: Koopman operator meets model predictive control. *Automatica*, 93:149–160, 2018.

Fuxian Li, Jie Feng, Huan Yan, Guangyin Jin, Fan Yang, Funing Sun, Depeng Jin, and Yong Li. Dynamic graph convolutional recurrent network for traffic prediction: Benchmark and solution. *ACM Transactions on Knowledge Discovery from Data*, 17(1):1–21, 2023.

Kunchang Li, Xinhao Li, Yi Wang, Yinan He, Yali Wang, Limin Wang, and Yu Qiao. VideoMamba: State space model for efficient video understanding. *arXiv preprint arXiv:2403.06977*, 2024.

Yunzhu Li, Hao He, Jiajun Wu, Dina Katabi, and Antonio Torralba. Learning compositional Koopman operators for model-based control. In *International Conference on Learning Representations*, 2020.

Opher Lieber, Barak Lenz, Hofit Bata, Gal Cohen, Jhonathan Osin, Itay Dalmedigos, Erez Safahi, Shaked Meirom, Yonatan Belinkov, Shai Shalev-Shwartz, et al. Jamba: A hybrid Transformer-Mamba language model. *arXiv preprint arXiv:2403.19887*, 2024.

TP Lillicrap. Continuous control with deep reinforcement learning. *arXiv preprint arXiv:1509.02971*, 2015.

Jinfeng Liu, David Muñoz de la Peña, Benjamin J Ohran, Panagiotis D Christofides, and James F Davis. A two-tier architecture for networked process control. *Chemical Engineering Science*, 63 (22):5394–5409, 2008.

Yong Liu, Chenyu Li, Jianmin Wang, and Mingsheng Long. Koopa: Learning non-stationary time series dynamics with Koopman predictors. In *Advances in Neural Information Processing Systems*, volume 36, pp. 12271–12290, 2023.

Bethany Lusch, J Nathan Kutz, and Steven L Brunton. Deep learning for universal linear embeddings of nonlinear dynamics. *Nature Communications*, 9(1):4950, 2018.

Jeremy Morton, Antony Jameson, Mykel J Kochenderfer, and Freddie Witherden. Deep dynamical modeling and control of unsteady fluid flows. In *Advances in Neural Information Processing Systems*, volume 31, 2018.

Eric Nguyen, Karan Goel, Albert Gu, Gordon Downs, Preey Shah, Tri Dao, Stephen Baccus, and Christopher Ré. S4nd: Modeling images and videos as multidimensional signals with state spaces. In *Advances in Neural Information Processing Systems*, volume 35, pp. 2846–2861, 2022.

M Nikravesh, AE Farell, and TG Stanford. Control of nonisothermal CSTR with time varying parameters via dynamic neural network control (DNNC). *Chemical Engineering Journal*, 76(1): 1–16, 2000.

Julian Nubert, Johannes Köhler, Vincent Berenz, Frank Allgöwer, and Sebastian Trimpe. Safe and fast tracking on a robot manipulator: Robust MPC and neural network control. *IEEE Robotics and Automation Letters*, 5(2):3050–3057, 2020.

Jiacheng Ruan and Suncheng Xiang. VM-UNet: Vision Mamba UNet for medical image segmentation. *arXiv preprint arXiv:2402.02491*, 2024.

Jan C Schulze, Danimir T Doncevic, and Alexander Mitsos. Identification of MIMO Wiener-type Koopman models for data-driven model reduction using deep learning. *Computers & Chemical Engineering*, 161:107781, 2022.

Haojie Shi and Max Q-H Meng. Deep Koopman operator with control for nonlinear systems. *IEEE Robotics and Automation Letters*, 7(3):7700–7707, 2022.

Aivar Sootla, Natalja Strelkowa, Damien Ernst, Mauricio Barahona, and Guy-Bart Stan. On periodic reference tracking using batch-mode reinforcement learning with application to gene regulatory network control. In *IEEE Conference on Decision and Control*, pp. 4086–4091, 2013.

Natalja Strelkowa and Mauricio Barahona. Switchable genetic oscillator operating in quasi-stable mode. *Journal of The Royal Society Interface*, 7(48):1071–1082, 2010.

Naoya Takeishi, Yoshinobu Kawahara, and Takehisa Yairi. Learning Koopman invariant subspaces for dynamic mode decomposition. In *Advances in Neural Information Processing Systems*, volume 30, 2017.

Peter Van Overschee and BL0888 De Moor. *Subspace identification for linear systems: Theory—Implementation—Applications*. Springer Science & Business Media, 2012.

Ashish Vaswani, Noam Shazeer, Niki Parmar, Jakob Uszkoreit, Llion Jones, Aidan N Gomez, Łukasz Kaiser, and Illia Polosukhin. Attention is all you need. In *Advances in Neural Information Processing Systems*, volume 30. Curran Associates, Inc., 2017.

Yogesh Verma, Markus Heinonen, and Vikas Garg. Climode: Climate and weather forecasting with physics-informed neural odes. In *International Conference on Learning Representations*, 2024.

Andreas Wächter and Lorenz T Biegler. On the implementation of an interior-point filter line-search algorithm for large-scale nonlinear programming. *Mathematical Programming*, 106(1): 25–57, 2006.

Kun Wang, Hao Wu, Yifan Duan, Guibin Zhang, Kai Wang, Xiaojiang Peng, Yu Zheng, Yuxuan Liang, and Yang Wang. Nuwadynamics: Discovering and updating in causal spatio-temporal modeling. In *International Conference on Learning Representations*, 2024.

Matthew O Williams, Ioannis G Kevrekidis, and Clarence W Rowley. A data–driven approximation of the Koopman operator: Extending dynamic mode decomposition. *Journal of Nonlinear Science*, 25:1307–1346, 2015.

Thomas Wolf, Lysandre Debut, Victor Sanh, Julien Chaumond, Clement Delangue, Anthony Moi, Pierric Cistac, Tim Rault, Rémi Louf, Morgan Funtowicz, Joe Davison, Sam Shleifer, Patrick von Platen, Clara Ma, Yacine Jernite, Julien Plu, Canwen Xu, Teven Le Scao, Sylvain Gugger, Mariama Drame, Quentin Lhoest, and Alexander M. Rush. Transformers: State-of-the-art natural language processing. In *Proceedings of the 2020 Conference on Empirical Methods in Natural Language Processing: System Demonstrations*, pp. 38–45, Online, 2020.

Xunyuan Yin and Jinfeng Liu. Subsystem decomposition of process networks for simultaneous distributed state estimation and control. *AIChE Journal*, 65(3):904–914, 2019.

Jing Zeng and Jinfeng Liu. Economic model predictive control of wastewater treatment processes. *Industrial & Engineering Chemistry Research*, 54(21):5710–5721, 2015.

Hao Zhang, Clarence W Rowley, Eric A Deem, and Louis N Cattafesta. Online dynamic mode decomposition for time-varying systems. *SIAM Journal on Applied Dynamical Systems*, 18(3): 1586–1609, 2019.

Xuewen Zhang, Minghao Han, and Xunyuan Yin. Reduced-order Koopman modeling and predictive control of nonlinear processes. *Computers & Chemical Engineering*, 179:108440, 2023.

Wayne Xin Zhao, Kun Zhou, Junyi Li, Tianyi Tang, Xiaolei Wang, Yupeng Hou, Yingqian Min, Beichen Zhang, Junjie Zhang, Zican Dong, et al. A survey of large language models. *arXiv preprint arXiv:2303.18223*, 2023.

Lianghui Zhu, Bencheng Liao, Qian Zhang, Xinlong Wang, Wenyu Liu, and Xinggang Wang. Vision Mamba: Efficient visual representation learning with bidirectional state space model. *arXiv preprint arXiv:2401.09417*, 2024.

A KOOPMAN OPERATOR

According to the approach discussed in (Korda & Mezić, 2018), a state vector incorporating both state and input can be defined as $\mathcal{X}_k = \left[x_k^{\mathrm{T}}, u_k^{\mathrm{T}}\right]^{\mathrm{T}}$. Defining a left shift operator $\mathcal{S}$ such that $\mathcal{S}u_k = u_{k+1}$, the dynamics of this augmented state vector can be expressed as follows:

$$\mathcal{X}_{k+1} = \mathcal{F}(\mathcal{X}_k) := \begin{bmatrix} f(x_k, u_k) \\ \mathcal{S}u_k \end{bmatrix} := \begin{bmatrix} f(x_k, u_k) \\ u_{k+1} \end{bmatrix} \tag{11}$$

The Koopman operator $\mathcal{K}_{\mathcal{F}} : \mathcal{H}_{\mathcal{F}} \to \mathcal{H}_{\mathcal{F}}$ for (11) governs the dynamics of the augmented vector $\mathcal{X}$ in a linear fashion:

$$\mathcal{K}_{\mathcal{F}}\Psi(\mathcal{X}_k) = \Psi \circ \mathcal{F}(\mathcal{X}_k) = \Psi(\mathcal{X}_{k+1}). \tag{12}$$

The observable functions inside Ψ transfer the original states into the higher-dimensional space.

In (Korda & Mezić, 2018), only the states are lifted to a higher-dimensional space, while no transformations are applied to the inputs. Specifically, the observable functions Ψ are defined as follows:

$$\Psi(\mathcal{X}_k) = \Psi(x_k, u_k) = \left[\psi^{\mathrm{T}}(x_k), u_k^{\mathrm{T}}\right]^{\mathrm{T}} \tag{13}$$

where $\psi : \mathbb{R}^n \to \mathbb{R}^N$ is the observable function that transforms the original states.

For real-world applications, a finite-dimensional approximation of the Koopman operator, denoted as $\mathcal{K}_{N_\phi}$, needs to be identified. Since future inputs are not considered, only the elements in the first N rows of the $\mathcal{K}_{N_\phi}$ need to be identified. The formulation of $\mathcal{K}_{N_\phi}$ can be expressed as:

$$\mathcal{K}_{N_\phi} = \left[\begin{array}{c:c} A & B \\ \hdashline * & * \end{array}\right] \tag{14}$$

where $A \in \mathbb{R}^{N \times N}$, $B \in \mathbb{R}^{N \times m}$. To capture the dynamics of $\mathcal{X}_k$, it is sufficient to identify only the matrices A and B in (14), while the blocks denoted by $*$ can be ignored.

B MAMBA FRAMEWORK

The matrices generation network in MamKO is inspired by the Mamba. It is worth noting that there are differences between our methods and the Mamba structure.

Firstly, the Mamba structure is designed for LLM with word sequences as inputs and generates corresponding word sequences. Instead, our method attempts to model real-world systems containing both states and inputs. Compared with LLM, our MamKO model is closer to the concept (Ha & Schmidhuber, 2018), which contains the interaction between states and actions.

Secondly, the matrices generation network of Mamba utilizes the information in the whole input sequence. Given the sequence $U_k = \{u_j\}_{j=k,\cdots,k+H-1}$, the matrices A_k, B_k and C_k in (5) are obtained from the nonlinear neural networks, which can be denoted as $A_k = f_{A_k}(U_k)$, $B_k = f_{B_k}(U_k)$. $C_k = f_{C_k}(U_k)$. The SSM from Mamba can be formulated as:

$$\begin{aligned} z_{k+1} &= f_{A_k}(U_k)z_k + f_{B_k}(U_k)u_k \\ \hat{x}_k &= f_{C_k}(U_k)z_k \end{aligned} \tag{15}$$

The nonlinear functions f_{A_k}, f_{B_k}, f_{C_k} and the bilinear terms $f_{A_k}(U_k)z_k$, $f_{B_k}(U_k)u_k$ make the relationship between z_k and u_k no longer linear. Applying MPC for this nonlinear system can cause non-convex optimization problems, which may reduce the control efficiency. In our work, the matrices are generated from historical data, which have no direct relationship between z_k and u_k. The linear relationship between z_k and c_k allows for the construction of convex optimization problems.

Lastly, the SSMs in the Mamba structure are separately generated for each channel of the input sequence. For the input $u \in \mathbb{R}^m$ with m channels, m pairs of SSMs with $A_k \in \mathbb{R}^{N \times N}$, $B_k \in \mathbb{R}^{N \times 1}$, $C_k \in \mathbb{R}^{1 \times N}$ matrices are generated at time instant k. The multiple pairs of SSMs are not directly applicable to MPC. In our framework, the SSMs are designed to describe the dynamics of all the input channels (features), which can be formulated as $A_k \in \mathbb{R}^{N \times N}$, $B_k \in \mathbb{R}^{N \times m}$, $C_k \in \mathbb{R}^{n \times N}$ for each time instant.

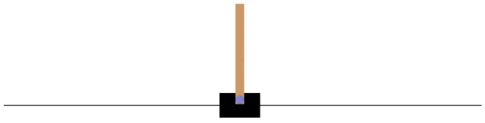

Figure 5: CartPole system.

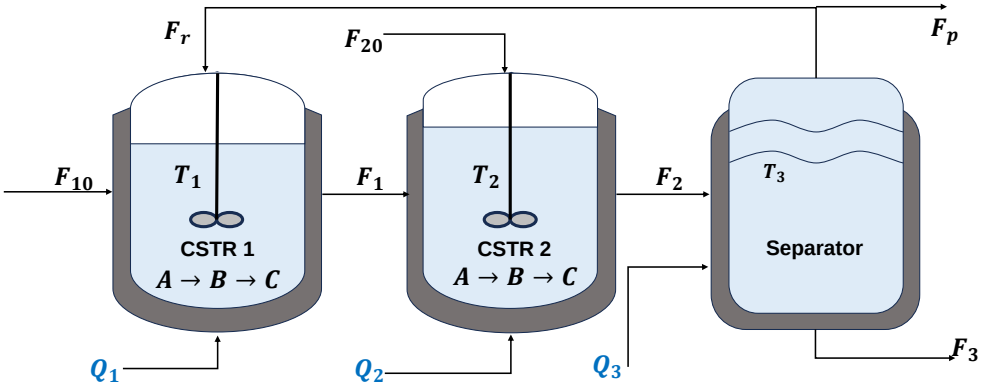

Figure 6: Time-invariant RSCP system (Liu et al., 2008).

C Experimental Setup

The experiments are set based on OpenAI Gym (Brockman et al., 2016). Part of the environments are presented in Figure 5 and Figure 6.

C.1 CartPole - Inverted Pendulum on a Cart

We modified the CartPole system described in (Brockman et al., 2016) using a continuous action space instead of a discrete one. The system consists of a cart that moves horizontally with an inverted pendulum attached to it. While the cart is fully actuated, the pendulum remains unactuated. In this experiment, the controller aims to keep the pendulum upright and vertical. The control input is the horizontal force applied to the cart ($a \in [-20, 20]$). $x_{\text{threshold}}$ and $\theta_{\text{threshold}}$ represents the maximum of position and angle, respectively, $x_{\text{threshold}} = 10$ and $\theta_{\text{threshold}} = 20°$. The episode ends if $|\theta| > \theta_{\text{threshold}}$ and the episodes end in advance. The episodes for control evaluation are of length 1000. For time-varying CartPole, the model is based on a modified system in (Hao et al., 2022), which can be presented as:

$$\begin{aligned}
\ddot{x}_t &= \frac{F_t + ml\left(\dot{\bar{\theta}}_t^2 \sin\bar{\theta}_t - \ddot{\bar{\theta}}_t \cos\bar{\theta}_t\right) - \mu_t^c \operatorname{sgn}(\dot{x}_t)}{m_c + m} \\
\ddot{\bar{\theta}}_t &= \frac{\cos\theta_t \left[-F_t - ml\dot{\bar{\theta}}_t^2 \sin\theta_t + \mu_t^c \operatorname{sgn}(\dot{x}_t)\right] / (m_c + m)}{l\left[\frac{4}{3} - \left(m\cos^2\bar{\theta}_t\right) / (m_c + m)\right]} + \frac{g\sin\theta_t - \mu_p\dot{\bar{\theta}}/ml}{l\left[\frac{4}{3} - \left(m\cos^2\bar{\theta}_t\right) / (m_c + m)\right]}
\end{aligned} \tag{16}$$

where $\mu_t^c = 0.0005 + cos(\omega t)$ is time-varying coefficient of friction of cart on the track; ω is the angular frequency of the sine wave; x_t is the distance to the initial position; $\bar{\theta}_t$ is the offset angle; $\dot{x}_t, \dot{\theta}_t$ is the velocity and the angular velocity respectively; F_t is the continuous control input. The parameters are set the same as the time-invariant CartPole, which can be presented as:

$$m_c = 1.0 \text{ kg}, m = 0.1 \text{ kg}, l = 0.5 \text{ m}$$

For the time-varying Cartpole system, the angular frequency is set as $\omega = 1$; for the rapidly changing dynamics, the angular frequency is set as $\omega = 0.1$, $\omega = 1$, $\omega = 10$, respectively.

Notably, the control tasks for the two systems include position control and angular control. The controller should stabilize the CartPole in the state that $x_t = 0$ and $\theta_t = 0$. The cost designed for the two CartPole systems is defined as:

$$cost_{cartpole}(x_t, \theta_t) = \frac{x_t^2}{100} + 180\frac{\theta_t^2}{\pi} \tag{17}$$

C.2 Synthetic Biology Gene Regulatory Networks

The gene regulatory networks (GRNs) discussed in this paper function at the nanoscale, demonstrating unique physical properties that distinguish them from other examples. Notably, these GRNs exhibit intriguing oscillatory behavior.

In this example, we focus on a classical dynamical system from systems and synthetic biology, specifically addressing a reference tracking task. The GRN under consideration is a synthetic three-gene regulatory network, where the dynamics of mRNAs and proteins inside the network exhibit oscillatory behavior. A detailed description of the network's mechanisms can be found in (Elowitz & Leibler, 2000). The discrete-time mathematical model of the GRNs can be represented by the following equations:

$$\begin{aligned}
x_1(t+1) &= x_1(t) + dt \cdot \left[-\gamma_1 x_1(t) + \frac{a_1}{K_1 + x_6^2(t)} + u_1\right] + \xi_1(t), \\
x_2(t+1) &= x_2(t) + dt \cdot \left[-\gamma_2 x_2(t) + \frac{a_2}{K_2 + x_4^2(t)} + u_2\right] + \xi_2(t), \\
x_3(t+1) &= x_3(t) + dt \cdot \left[-\gamma_3 x_3(t) + \frac{a_3}{K_3 + x_5^2(t)} + u_3\right] + \xi_3(t), \\
x_4(t+1) &= x_4(t) + dt \cdot [-c_1 x_4(t) + \beta_1 x_1(t)] + \xi_4(t), \\
x_5(t+1) &= x_5(t) + dt \cdot [-c_2 x_5(k) + \beta_2 x_2(t)] + \xi_5(t), \\
x_6(t+1) &= x_6(t) + dt \cdot [-c_3 x_6(t) + \beta_3 x_3(t)] + \xi_6(t).
\end{aligned} \tag{18}$$

In this context, x_1, x_2, x_3 represent the concentrations of the mRNA transcripts, and x_4, x_5, x_6 represent the concentrations of the corresponding proteins for genes 1, 2, and 3, respectively. The terms ξ_i, for all i, are independent and identically distributed. Uniform noise variables are drawn from the range $[-\delta, \delta]$. For the simulations described in Section 5, δ is set to 0, while for the robustness tracking task in F.6, δ is set to 0.5. The parameters a_1, a_2, and a_3 indicate the highest promoter strengths for the respective genes. The symbols γ_1, γ_2, and γ_3 represent the degradation rates of mRNA, whereas c_1, c_2, and c_3 correspond to the degradation rates of proteins. Moreover, β_1, β_2, and β_3 denote the protein synthesis rates, and K_1, K_2, and K_3 are the associated dissociation constants. The equations in (18) present a network structure in which gene 1 is inhibited by gene 2, gene 2 is suppressed by gene 3, and gene 3, in turn, is repressed by gene 1. The discretization time step is denoted by dt. The protein concentrations are observable and are typically measured using fluorescent markers, such as green fluorescent protein (GFP) or red fluorescent protein (mCherry). The control inputs u_i are applied via light control signals, which activate photo-sensitive promoters to induce gene expression. In line with the standard practice of GRN models in (Elowitz & Leibler, 2000), we simplify the system dynamics by assuming that the parameters regulating mRNA and protein dynamics are uniform across all genes. Further details on the mathematical modeling and control of synthetic gene regulatory networks can be found in (Strelkowa & Barahona, 2010; Sootla et al., 2013). In the simulations mentioned in this paper, the parameters are chosen as follows:

$$\forall i: \ K_i = 1, a_i = 1.6, \gamma_i = 0.16, \beta_i = 0.16, c_i = 0.06, dt = 1$$

For the tracking task for x_4, the cost function for the GRN system is defined as:

$$cost_{GRN}(x_4) = (x_4 - 6)^2 \tag{19}$$

C.3 Reactor-separator process

A reactor-separator process, consisting of two continuous stirred tank reactors (CSTRs) and a flash tank separator (Liu et al., 2008), is considered in this paper. A schematic of the process is shown in

Figure 6. The process consists of two chemical reactions: firstly, the reactant A is transformed into the desired product B, followed by a secondary reaction where a fraction of B is further converted into the byproduct C. The system starts with the pure reactant A being fed into the first reactor (CSTR 1) at a flow rate of F_{10}. The output stream from CSTR 1, with a flow rate of F_1, together with an additional fresh supply of pure A at a rate of F_{20}, enters CSTR 2. The outflow from CSTR 2 is then directed to the separator at a flow rate of F_2. Within the separator, a recycle stream with a flow rate of F_r is redirected back to the first reactor for further conversion. All three vessels (CSTR 1, CSTR 2, and the separator) are equipped with a jacket to provide or remove heat, with a heating input rate Q_i, where $i = 1, 2, 3$. The system's ordinary differential equations can be expressed as follows (Liu et al., 2008; Yin & Liu, 2019):

$$
\begin{aligned}
\frac{dx_{A1}}{dt} &= \frac{F_{10}}{V_1}(x_{A10} - x_{A1}) + \frac{F_r}{V_1}(x_{Ar} - x_{A1}) - \phi_c k_1 e^{\frac{-E_1}{rT_1}} x_{A1} \\
\frac{dx_{B1}}{dt} &= \frac{F_{10}}{V_1}(x_{B10} - x_{B1}) + \frac{F_r}{V_1}(x_{Br} - x_{B1}) + \phi_c k_1 e^{\frac{-E_1}{rT_1}} x_{A1} - \phi_c k_2 e^{\frac{-E_2}{rT_1}} x_{B1} \\
\frac{dT_1}{dt} &= \frac{F_{10}}{V_1}(T_{10} - T_1) + \frac{F_r}{V_1}(T_3 - T_1) - \phi_c \frac{\Delta H_1}{c_p} k_1 e^{\frac{-E_1}{rT_1}} x_{A1} - \phi_c \frac{\Delta H_2}{c_p} k_2 e^{\frac{-E_2}{rT_1}} x_{B1} + \frac{Q_1}{\rho c_p V_1} \\
\frac{dx_{A2}}{dt} &= \frac{F_1}{V_2}(x_{A1} - x_{A2}) + \frac{F_{20}}{V_2}(x_{A20} - x_{A2}) - \phi_c k_1 e^{\frac{-E_1}{rT_2}} x_{A2} \\
\frac{dx_{B2}}{dt} &= \frac{F_1}{V_2}(x_{B1} - x_{B2}) + \frac{F_{20}}{V_2}(x_{B20} - x_{B2}) + \phi_c k_1 e^{\frac{-E_1}{rT_2}} x_{A2} - \phi_c k_2 e^{\frac{-E_2}{rT_2}} x_{B2} \\
\frac{dT_2}{dt} &= \frac{F_1}{V_2}(T_1 - T_2) + \frac{F_{20}}{V_2}(T_{20} - T_2) - \phi_c \frac{\Delta H_1}{c_p} k_1 e^{\frac{-E_1}{rT_2}} x_{A2} - \phi_c \frac{\Delta H_2}{c_p} k_2 e^{\frac{-E_2}{rT_2}} x_{B2} + \frac{Q_2}{\rho c_p V_2} \\
\frac{dx_{A3}}{dt} &= \frac{F_2}{V_3}(x_{A2} - x_{A3}) - \frac{(F_r + F_p)}{V_3}(x_{Ar} - x_{A3}) \\
\frac{dx_{B3}}{dt} &= \frac{F_2}{V_3}(x_{B2} - x_{B3}) - \frac{(F_r + F_p)}{V_3}(x_{Br} - x_{B3}) \\
\frac{dT_3}{dt} &= \frac{F_2}{V_3}(T_2 - T_3) + \frac{Q_3}{\rho c_p V_3} + \frac{(F_r + F_p)}{\rho c_p V_3}(x_{Ar}\Delta H_{\text{vap1}} + x_{Br}\Delta H_{\text{vap2}} + x_{Cr}\Delta H_{\text{vap3}})
\end{aligned}
\tag{20}
$$

For a more detailed explanation of this process, refer to (Liu et al., 2008; Yin & Liu, 2019). Additional process disturbances are introduced into the systems to evaluate the robustness of the proposed control strategy. These disturbances are sampled from a multivariate normal distribution $\mathcal{N}(\mathbf{0}, \sigma_\epsilon^2)$, where $\sigma_\epsilon = [0.01, 0.01, 0.50, 0.01, 0.01, 0.50, 0.01, 0.01, 0.50]$ corresponds to the standard deviations associated with the nine state variables. For time-invariant RSCP, parameter ϕ_c is set as $\phi_c = 1$; For time-varying, parameter ϕ_c is set as $\phi_c = e^{-0.01t}$. The control objectives for both processes are to regulate the system states and ensure the states remain at a steady-state set point:

$$x_s = [0.18, 0.67, 480.32\,\text{K}, 0.20, 0.65, 472.79\,\text{K}, 0.07, 0.67, 474.89\,\text{K}]^{\text{T}}$$

Given a set of scaling coefficients $x_{scale} = [0.36, 0.18, 361.94\,\text{K}, 0.21, 0.18, 342.88\,\text{K}, 0.26, 0.21, 361.59\,\text{K}]^{\text{T}}$, the cost function for the two RSCP systems can be defined as:

$$cost_{RSCP}(x) = (\frac{x - x_s}{x_{scale}})^2 \tag{21}$$

D HYPERPARAMETERS

The hyperparameters for the MamKO, DKO, and MLP are listed in Table 4, Table 5, Table 6, respectively.

Table 4: Hyperparameters of MamKO

Hyperparameters	**Value**
Size of training set	40000
Size of test set	4000
Batch Size	256
Learning rate	1e-3
Prediction horizon H	30
Structure of ψ (CartPole & Time-varying CartPole)	(4, 64, 8)
Structure of ψ (GRN)	(6, 64, 10)
Structure of ψ (Time-invariant RSCP & Time-varying RSCP)	(9, 64, 15)
Activation function in ψ	ReLU
Kernel size h of ϕ (CartPole)	10
Kernel size h of ϕ (Time-varying CartPole)	15
Kernel size h of ϕ (GRN)	10
Kernel size h of ϕ (Time-invariant RSCP)	10
Kernel size h of ϕ (Time-varying RSCP)	5
Dimension of observables (CartPole & Time-varying CartPole)	8
Dimension of observables (GRN)	10
Dimension of observables (time-invariant RSCP & Time-varying RSCP)	15

Table 5: Hyperparameters of DKO

Hyperparameters	**Value**
Size of training set	40000
Size of test set	4000
Batch Size	256
Learning rate	1e-3
Prediction horizon H	30
Structure of ψ (CartPole & Time-varying CartPole)	(4, 64, 8)
Structure of ψ (GRN)	(6, 64, 10)
Structure of ψ (Time-invariant RSCP & Time-varying RSCP)	(9, 64, 15)
Activation function	ReLU
Dimension of observables (CartPole & Time-varying CartPole)	8
Dimension of observables (GRN)	10
Dimension of observables (Time-invariant RSCP & Time-varying RSCP)	15

Table 6: Hyperparameters of MLP

Hyperparameters	**Value**
Size of training set	40000
Size of test set	4000
Batch Size	256
Learning rate	1e-3
Prediction horizon H	30
Structure of ϕ (CartPole & Time-varying CartPole)	(4, 24, 16, 8)
Structure of ϕ (GRN)	(6, 30, 20, 10)
Structure of ϕ (Time-invariant RSCP & Time-varying RSCP)	(9, 45, 30, 15)
Activation function	ReLU

E MODELING RESULTS

E.1 COMPARISION WITH CLASSIC SYSTEM IDENTIFICATION METHOD

A classical system identification method – subspace identification (Van Overschee & De Moor, 2012) is also applied to build a data-based dynamic model for the dynamics of the CartPole system. For the 30-step-ahead prediction task, the model built based on subspace identification can only provide satisfactory predictions of the position and velocity of the cart, while the predictions of the state variables related to the pole diverge. In contrast, the proposed method can accurately forecast the future behaviors of all the states of the CartPole system.

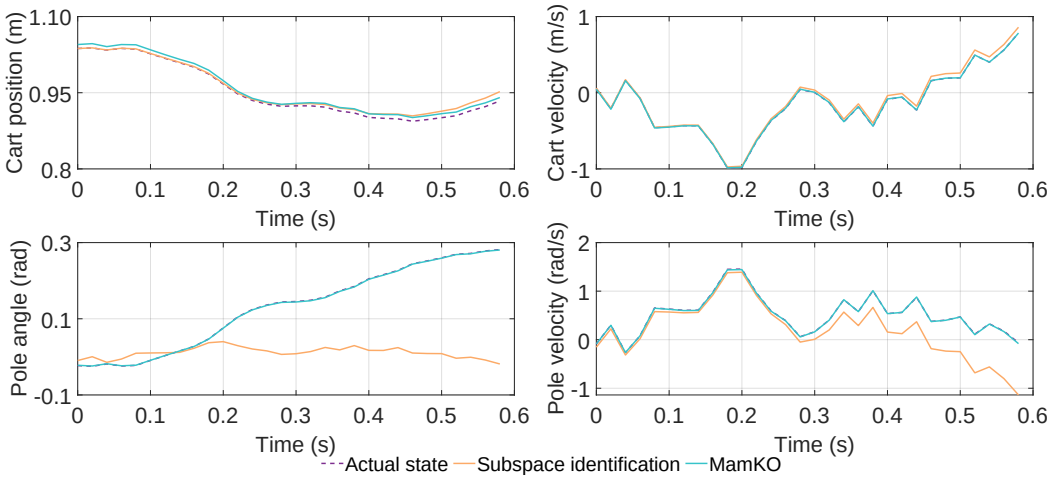

Figure 7: Modeling results of the CartPole system by MamKO and subspace identification.

E.2 THE SELECTION OF THE DIMENSION OF THE STATE-SPACE MODEL

The dimension of the linear state-space model is determined through trial and error. A case study on the CartPole system is conducted to illustrate the selection of the dimension of the state-space model. The results, which include the test loss across various lifting dimensions, are presented in Table 7. As the dimension of the lifted space increases from 5 to 8, the test loss decreases significantly to 6.93×10^{-4}. Further increasing the dimension does not lead to significant improvement in the modeling performance.

Table 7: Test loss of different lifting dimensions on CartPole system modeling by MamKO.

Lifting dimension	**5**	**8**	**10**	**15**
Test loss	8.95×10^{-4}	6.93×10^{-4}	6.94×10^{-4}	7.04×10^{-4}

E.3 PREDICTION ERROR ON EACH PREDICTION STEP

The modeling performance of the proposed method at each prediction step is evaluated. The results for the CartPole system, GRN system, and time-invariant RSCP system are presented in Figure 8, Figure 9, and Figure 10. From the results, it can be demonstrated that while the prediction error tends to increase as the number of prediction steps progresses, there is a notable reduction in error observed mid-way through the prediction horizon. This phenomenon underscores the effectiveness of our method in managing error propagation.

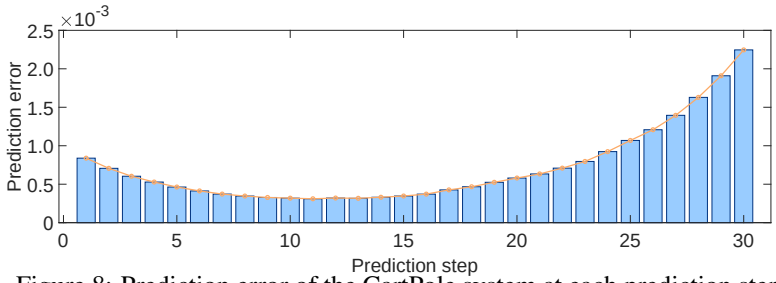

Figure 8: Prediction error of the CartPole system at each prediction step.

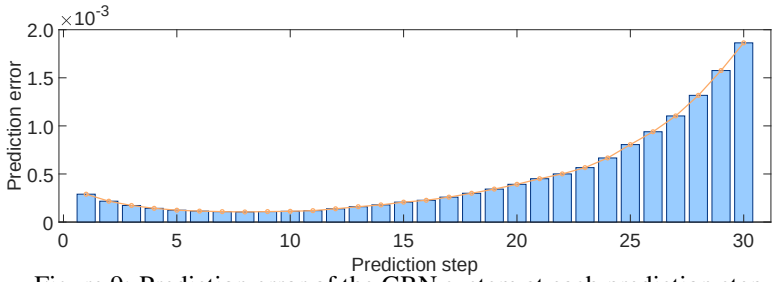

Figure 9: Prediction error of the GRN system at each prediction step.

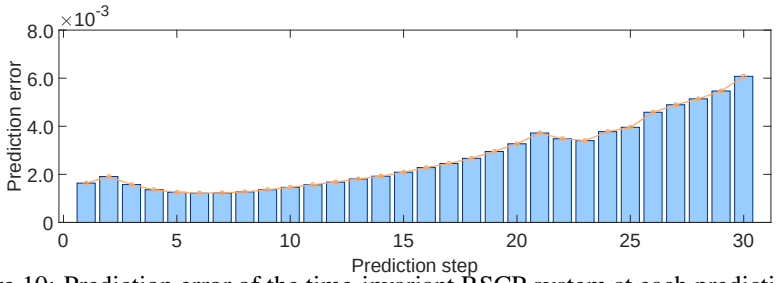

Figure 10: Prediction error of the time-invariant RSCP system at each prediction step.

F CONTROL EXPERIMENT RESULTS

F.1 CARTPOLE AND TIME-VARYING CARTPOLE SYSTEMS

The trajectories of the x and θ for the Cartpole systems are presented in Figure 11.

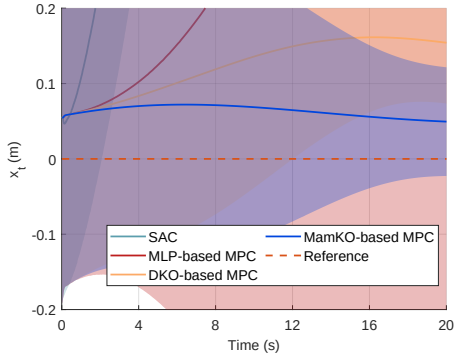

(a) x_t of the CartPole system

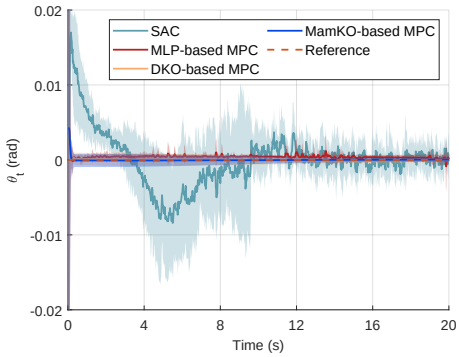

(b) θ_t of the CartPole system

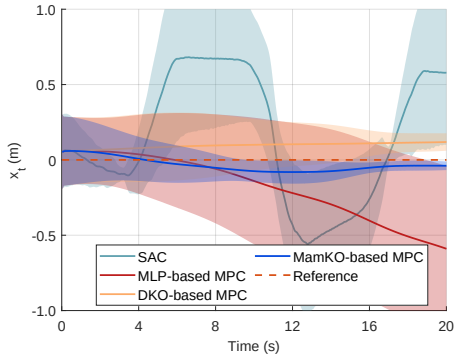

(c) x_t of the time-varying CartPole system

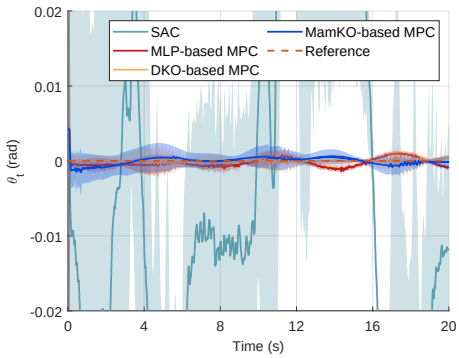

(d) θ_t of the time-varying CartPole system

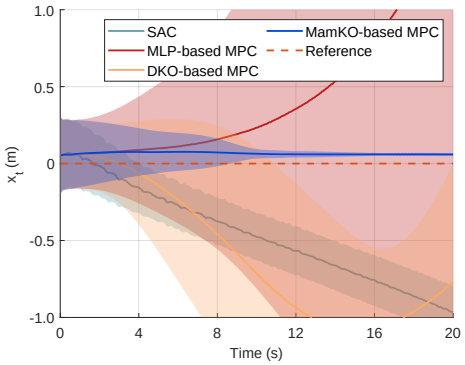

(e) x_t of the time-varying CartPole system with rapidly changing parameters

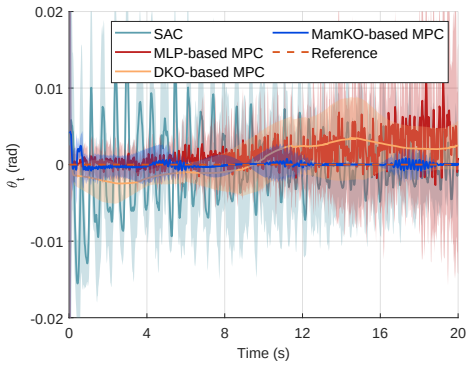

(f) θ_t of the time-varying CartPole system with rapidly changing parameters

Figure 11: The trajectories of the Cartpole systems. The Y-axis indicates the average state trajectory of each time instant. The shaded area represents the confidence interval (one standard deviation) over the ten experiments.

The steady-state errors of the three CartPole systems are listed in Table 8. From the results, the MamKO-based MPC demonstrates the smallest steady-state errors in all the states of each of the three CartPole systems. Particularly, for the time-varying CartPole system with rapidly changing parameters, the MamKO-based MPC achieves a substantial reduction in the steady-state error in

cart position, outperforming the MLP-based MPC, DKO-based MPC and SAC by 98.38%, 92.92%, and 93.86%, respectively.

Table 8: Steady-state errors of the three CartPole systems by different control methods.

Method	CartPole system		Time-varying CartPole system		CartPole system CartPole system with rapidly changing paramters	
	Cart position (m)	Pole angle (rad)	Cart position (m)	Pole angle (rad)	Cart position (m)	Pole angle (rad)
MamKO-based MPC	6.40×10^{-2}	2.15×10^{-4}	3.98×10^{-2}	4.74×10^{-3}	5.94×10^{-2}	2.96×10^{-4}
MLP-based MPC	1.28	5.26×10^{-4}	6.62×10^{-1}	1.02×10^{-3}	3.66	1.03×10^{-2}
DKO-based MPC	1.54×10^{-1}	2.35×10^{-4}	1.30×10^{-1}	5.14×10^{-3}	8.39×10^{-1}	2.68×10^{-3}
SAC	6.94×10^{-1}	1.92×10^{-2}	7.34×10^{-1}	1.87×10^{-2}	9.67×10^{-1}	2.65×10^{-2}

F.2 GRN SYSTEM

The trajectories of x_4 of the GRN system obtained based on different control methods are presented in Figure 12. The steady-state errors of the GRN system are listed in Table 9 .The proposed MamKO-based MPC provides the smallest steady-state error, reducing it by 52.23%, 92.10% and 90.68% as compared to MLP-based MPC, DKO-based MPC, and SAC, respectively.

Table 9: Steady-state error of the GRN system by different control methods.

Method	**MamKO-based MPC**	**MLP-based MPC**	**DKO-based MPC**	**SAC**
Steady-state error	5.35×10^{-2}	1.12×10^{-1}	6.77×10^{-1}	5.74×10^{-1}

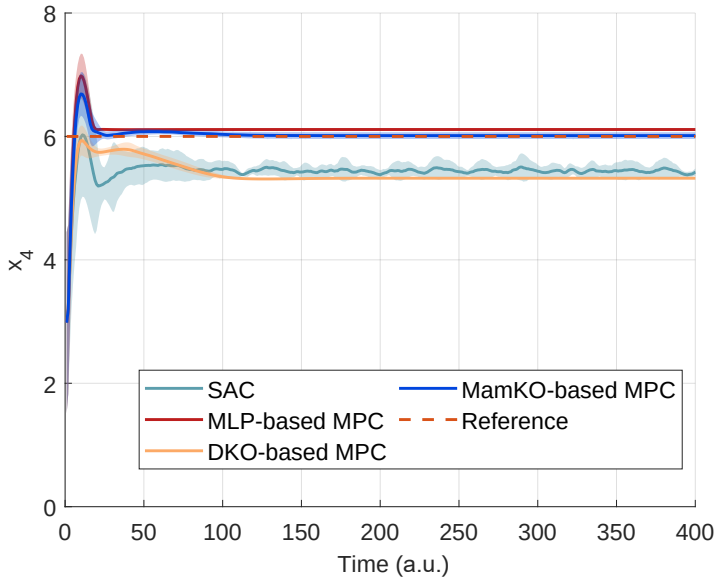

Figure 12: The trajectories of the GRN system by different control methods. The Y-axis indicates the average state trajectory of each time instant. The shaded area represents the confidence interval (one standard deviation) over the ten experiments

F.3 TIME-INVARIANT RSCP AND TIME-VARYING RSCP

One set of trajectories obtained from ten experiments for the time-invariant RSCP system is presented in Figure 13. One set of trajectories obtained from the ten experiments for the time-varying RSCP system is presented in Figure 14. Since the nine states of the RSCP system have significantly different magnitudes, the tracking errors for the RSCP system are calculated based on the states after normalization. The steady-state errors of the time-invariant RSCP system and time-varying RSCP system are listed in Table 10. From the results, the proposed MamKO-based MPC demonstrates the smallest steady-state error. For the time-invariant RSCP system, the proposed MamKO-based MPC achieves reductions in the steady-state error by 57.33%, 17.42%, and 61.68% as compared to MLP-based MPC, DKO-based MPC, and SAC, respectively. For the time-varying RSCP system, the proposed MamKO-based MPC reduces steady-state error by 49.78%, 24.83%, and 22.25% as compared to MLP-based MPC, DKO-based MPC, and SAC, respectively.

Table 10: Steady-state errors of the time-invariant RSCP system and the time-varying RSCP system.

Method	**MamKO-based MPC**	**MLP-based MPC**	**DKO-based MPC**	**SAC**
Time-invariant RSCP system	1.28×10^{-2}	3.00×10^{-2}	1.55×10^{-2}	3.34×10^{-2}
Time-varying RSCP system	6.78×10^{-2}	1.35×10^{-1}	9.02×10^{-2}	8.72×10^{-2}

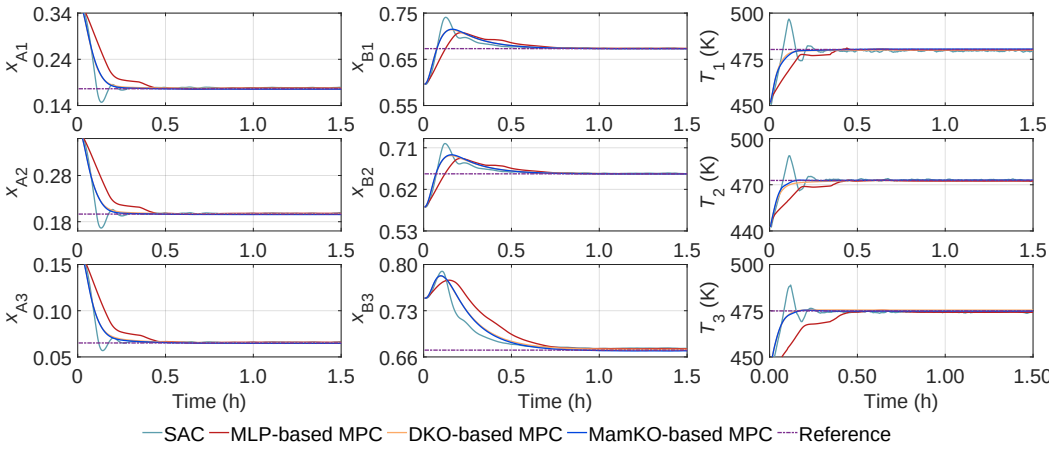

Figure 13: The state trajectories for the time-invariant RSCP systems.

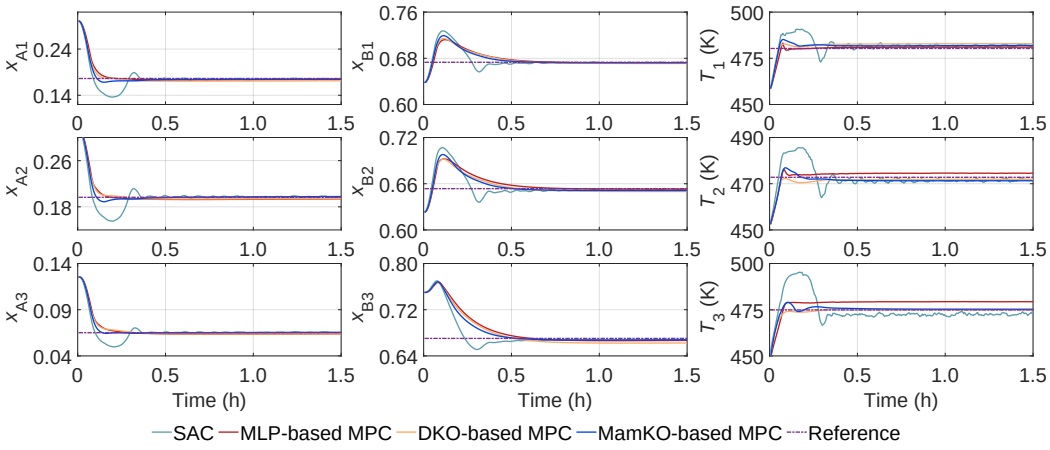

Figure 14: The state trajectories for the time-varying RSCP systems.

F.4 WATEWATER TREATMENT SYSTEM

To further demonstrate the applicability of the proposed method on highly nonlinear systems, we evaluate the performance of MamKO on a large-scale nonlinear water treatment system (Alex et al., 2008), which contains 145 states, two control inputs and 14 known disturbances. The dynamic behaviors of this process are simulated using a high-fidelity simulator that was built based on 145 ordinary differential equations (ODEs) (Zeng & Liu, 2015). A schematic of the water treatment plant is presented in Figure 15.

15 invariant states are excluded from Koopman-based modeling and control tasks. The modeling task aims to build a Koopman model that describes the evolution of the remaining 130 state variables over a 10-step prediction horizon. For the water treatment system, trajectories of state and action samples are gathered, generating a training set of $20,000$ samples, a validation set of $2,000$ samples, and a test set of $2,000$ samples. The modeling performance of the MamKO method and two baseline methods are presented in Figure 16. From the experimental results, the proposed method outperforms the deep Koopman operator (DKO) and multilayer perception (MLP) methods in modeling performance.

A set-point tracking task is considered to evaluate the control performance of the proposed method. The objective of the control task is to drive two selected states to a desired set point under the influence of the disturbances. In the control task, a PID controller and an MPC based on the first-principles model denoted as NMPC are included as the baselines. From the experimental results, the proposed MamKO-based MPC reduces tracking error by 55.60%, 45.95%, and 10.07% as compared to MLP-based MPC, DKO-based MPC, and SAC, respectively. The MPC based on the exact first-principles model (the same model as the simulator) exhibits the smallest tracking error. However, as emphasized in the introduction, obtaining an exact first-principles model can be challenging. Additionally, the nonlinear optimization required for first-principles model systems often results in suboptimal solutions, leading to large deviation points in the process. Our method achieves a reduction in tracking error of 11.56% as compared to the PID controller. Furthermore, integrating state constraints with the PID controller for this system can be challenging, and switching to a different set point may require retuning the parameters.

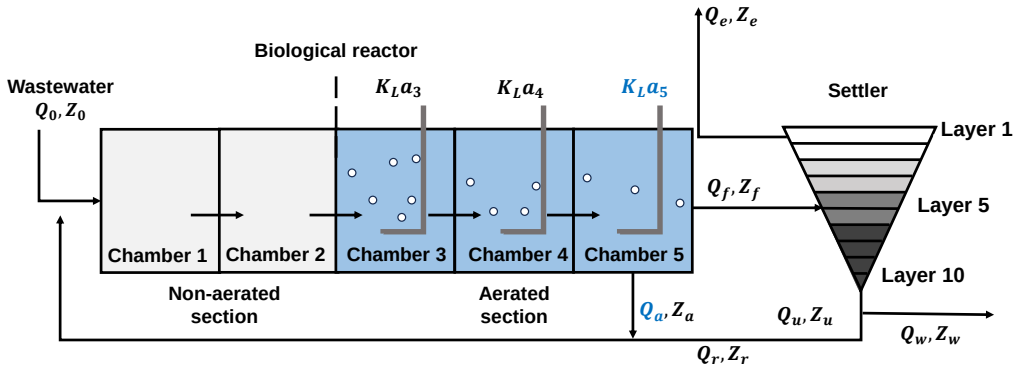

Figure 15: A schematic of the water treatment plant (Alex et al., 2008).

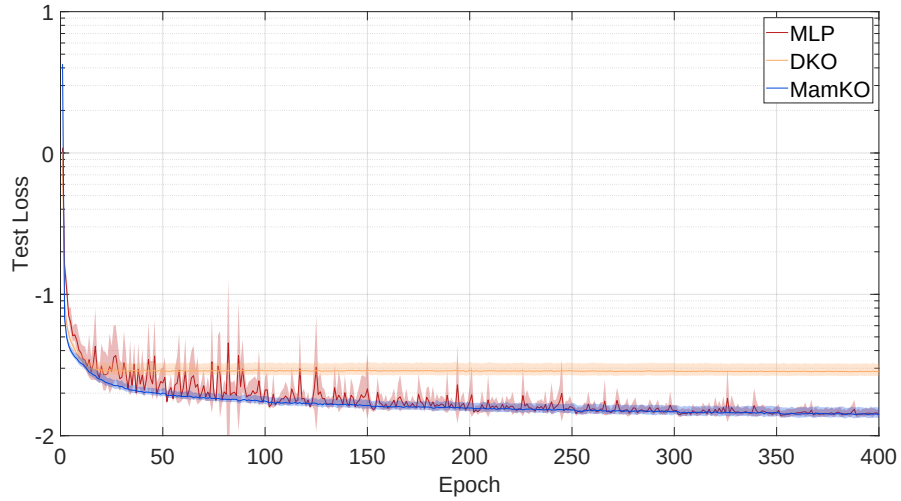

Figure 16: Test loss of water treatment process in log space from different methods. The shaded area represents the confidence interval (0.5 times the standard deviation) across ten training trials.

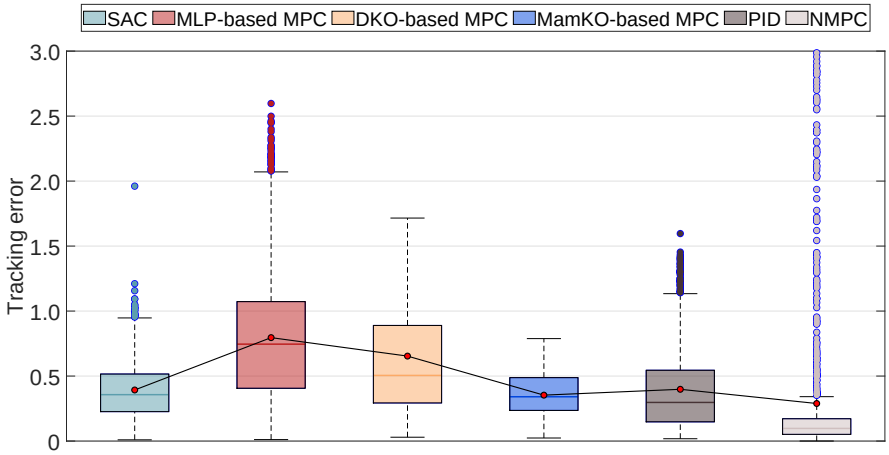

Figure 17: Tracking errors of the control task in the water treatment process from different methods. The red dots inside the boxes indicate the mean tracking errors in the process. The box chart shows the distribution of the tracking error. The middle line inside the box represents the median value of the collected data. The box represents the interquartile range (IQR), which encompasses the range between the first quartile (Q1) and the third quartile (Q3). The whiskers extend to the smallest and largest values within 1.5 times the IQR from the lower and upper quartiles. The outliers are the individual data points outside the whiskers.

F.5 TIME-DELAY RSCP SYSTEM

From the application perspective of the RSCP system, the transportation lag of reactant A and desired product B may introduce time delays in measuring the mass fractions x_{Ai} and x_{Bi}. In this system, a 0.025 h time delay is included. At each new sampling instant k, the controller optimizes control output based on the measurements of x_{Ai} and x_{Bi} at sampling instant $k-5$, instantaneous measurements of T_i and the historical trajectory. The modeling and control tasks of the time-delay RSCP system are the same as the time-invariant RSCP and time-varying RSCP system in Section 5. The modeling performance of each method is presented in Figure 18, and the control performance of each method is presented in Figure 19. From the results of modeling tasks, the proposed method reduces the test loss by 55.56% and 66.67% as compared with the MLP and DKO methods, respectively. For the control task, the proposed MamKO-based MPC reduces the cost by 52.52%, 53.59%, and 84.25% as compared to MLP-based MPC, DKO-based MPC, and SAC, respectively.

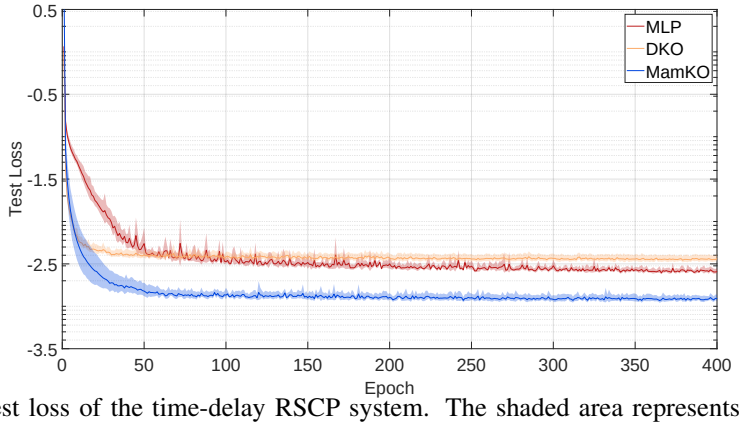

Figure 18: Test loss of the time-delay RSCP system. The shaded area represents the confidence interval (0.5 times the standard deviation) across ten training trials.

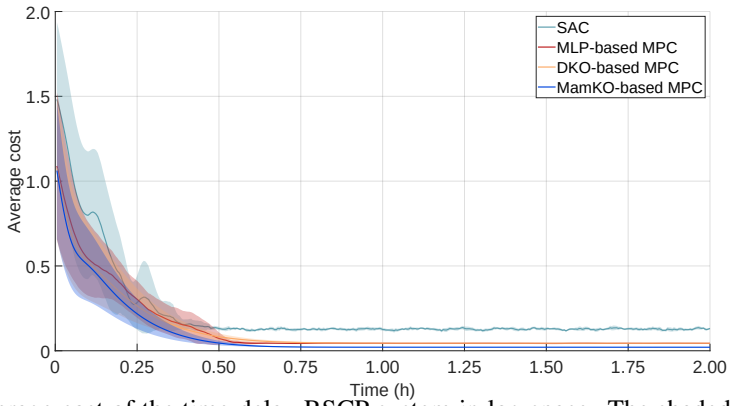

Figure 19: Average cost of the time-delay RSCP system in log space. The shaded area represents the confidence interval (0.3 times the standard deviation) over the ten experiments.

F.6 TRAJECTORY TRACKING TASK FOR GRN SYSTEM

A sinusoidal function with periods of 400 seconds is set as the tracking target of the task, which can be represented as:

$$x(t) = 5\sin\left(\frac{\pi}{200}t\right) + 10 \tag{22}$$

In the tracking process, extra uniform disturbance ranging from $[-0.5, 0.5]$, i.e., $\xi_i \sim \mathcal{U}(-0.5, 0.5)$ is added in the tracking process. The tracking trajectories of the GRN system are shown in Figure 20. The mean tracking errors of the different methods are presented in Table 11. From the results, the MamKO-based MPC exhibits the best tracking performance among the control methods, which reduces the tracking error by 9.84%, 20.29%, 32.93% as compared to MLP-based MPC, DKO-based MPC, and SAC, respectively. The experimental results demonstrate that the proposed method can be applied to trajectory-tracking tasks.

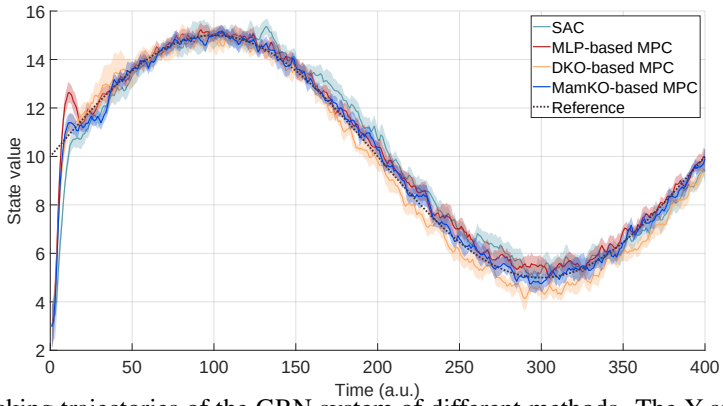

Figure 20: Tracking trajectories of the GRN system of different methods. The Y-axis indicates the average state trajectory of each time instant. The shaded area represents the confidence interval (one standard deviation) over the ten experiments.

Table 11: Mean tracking errors of GRN system of different methods.

System	MamKO-based MPC	MLP-based MPC	DKO-based MPC	SAC
Mean tracking error	0.55	0.61	0.69	0.82